photonics

MDPI

Article

THz Mixing with High-T_C Hot Electron Bolometers: A Performance Modeling Assessment for Y-Ba-Cu-O Devices

Romain Ladret [1], Annick Dégardin [1], Vishal Jagtap [1,2] and Alain Kreisler [1,*]

[1] CentraleSupélec, CNRS, Univ. Paris-Sud, Université Paris-Saclay, Sorbonne Université, Group of Electrical Engineering, GeePs, 91190 Gif sur Yvette, France; romain.ladret@gmail.com (R.L.); annick.degardin@centralesupelec.fr (A.D.); vishal.jagtap@centralesupelec.fr (V.J.)

[2] Institute for High Frequency and Communication Technology, University of Wuppertal, D-42119 Wuppertal, Germany; jagtap@uni-wuppertal.de

* Correspondence: alain.kreisler@centralesupelec.fr; Tel.: +33-1-6985-1651

Received: 15 December 2018; Accepted: 24 January 2019; Published: 25 January 2019

Abstract: Hot electron bolometers (HEB) made from high-T_C superconducting $YBa_2Cu_3O_{7-x}$ (YBCO) oxide nano-constrictions are promising THz mixers, due to their expected wide bandwidth, large mixing gain, and low intrinsic noise. The challenge for YBCO resides, however, in the chemical reactivity of the material and the related aging effects. In this paper, we model and simulate the frequency dependent performance of YBCO HEBs operating as THz mixers. We recall first the main hypotheses of our hot spot model taking into account both the RF frequency effects in the YBCO superconducting transition and the nano-constriction impedance at THz frequencies. The predicted performance up to 4 THz is given in terms of double sideband noise temperature T_{DSB} and conversion gain G. At 2.5 THz for instance, $T_{DSB} \cong 1000$ K and $G \cong -6$ dB could be achieved at 12.5 μW local oscillator power. We then consider a standoff target detection scheme and examine the feasibility with YBCO devices. For instance, detection at 3 m through cotton cloth in passive imaging mode could be readily achieved in moderate humidity conditions with 10 K resolution.

Keywords: THz heterodyne mixer; hot electron bolometer; Y-Ba-Cu-O high-T_C superconductor; hot spot model; RF local power distribution; THz impedance; noise temperature; conversion loss; standoff detection prediction; passive imaging

1. Introduction

First considered by Gershenzon et al. [1], the superconducting hot electron bolometer (HEB) principle was applied by these authors to low-T_C (T_C is the superconducting critical temperature) and high-T_C HEBs, Nb and $YBa_2Cu_3O_{7-x}$ (with x lower than 0.2, and called YBCO hereafter), respectively. The concept then fruitfully evolved [2], rather in favor of low T_C devices to start with, mainly Nb and NbN, exhibiting the diffusion cooled and phonon cooled processes, respectively [3]. In fact, the research on HEBs was mainly driven by immediate applications to THz radio astronomy as mixers for heterodyne reception [4,5]. Besides, YBCO was attractive in several respects, e.g., operating temperature with light cryogenics, or fast response, due to its very short electron-phonon relaxation time τ_{ep}, in the ps range [6–8]. Early YBCO HEB mixers were demonstrated at mm-wave [9–12] or THz [9,10,13–15] frequencies. Difficulties were encountered, however, which mainly arose from YBCO chemical reactivity to atmospheric water and carbon dioxide and to the fabrication process as well, which compromised the durability of good performances for frequency mixing operation [16]. They also arose from the superconducting film to substrate phonon escape time τ_{esc}, much longer for YBCO [17] than for Nb, for instance [18], with a detrimental effect on the instantaneous

bandwidth [11–13,19]. More recently, MgB_2 has met a sustained interest as a compromise between NbN and YBCO, in terms of operating temperature, but also in terms of instantaneous bandwidth [20,21].

The just mentioned experimental work was permanently sustained by modeling and simulation efforts to predict and interpret HEB performance. We now introduce those performance simulation aspects, because they indeed are our main concern in the present article.

Several steps in the HEB modeling approach have to be considered. In the "0D" or point bolometer model, only energy transfer between thermal reservoirs is evaluated. In the superconducting material (Figure 1a), the electron reservoir at temperature T_e interacts with the phonon reservoir at temperature T_p; this interaction is governed by the above-mentioned electron-phonon relaxation time τ_{ep}. The phonons release their energy to the device substrate with the above-mentioned escape time τ_{esc} [22]. If the electron-electron interaction time τ_{ee} is much shorter than τ_{ep}, (which is the case for Nb, NbN or YBCO), hot electron bolometric action occurs, such that $T_e > T_p$, provided that $\tau_{esc} << \tau_{ep}$. This latter condition is related to the film-substrate interface quality, which is mainly correlated with the device technological elaboration process. As a further refinement of this model, a three thermal reservoir model can be considered, including the substrate to the cold finger thermal resistance [23]; although 0D, this latter model also discusses the dimensions of the device constriction to achieve good sensitivity HEBs. As shown in Figure 1b, the constriction is defined by its length L, width w and thickness θ.

Further modeling developments took the HEB device geometry into account to describe the electron temperature profile $T_e(x)$ with respect to the constriction length coordinate ($0 < x < L$). First developed for low T_C HEBs [24], this so-called "hot spot" modeling was further applied to high T_C devices [25]. The YBCO HEB model then evolved to include more realistic descriptions, such as the phonon temperature spatial dependence $T_p(x)$ [26] and the operating radio frequency (RF) influence on the shape of the resistance vs. temperature superconducting transition [27].

The aim of this article is twofold. First, we shall provide a complete and detailed description of the YBCO HEB model and extend the results of [25–27] up to 4 THz. We shall also compare our modeling results in terms of the device performance as a THz heterodyne mixer with the few experimental data available for YBCO HEB mixers, which can be found in the literature.

Second, we shall consider the potential of such a device to provide a lightweight system for THz standoff detection for such applications as security and control. We shall therefore evaluate the standoff detection limits using passive imaging with YBCO HEB mixers. In this framework, we shall simulate well-defined and credible scenarios in terms of target distance, temperature resolution, atmospheric relative humidity, and transmission through clothing.

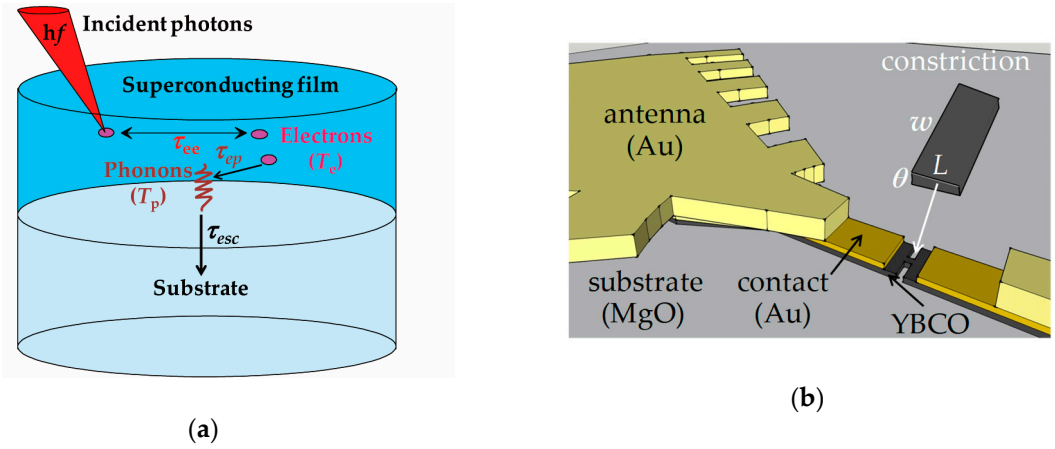

Figure 1. Superconducting hot electron bolometers (HEB): (**a**) Illustration of the point bolometer thermal model with two-reservoirs (electrons and phonons of the superconductor); (**b**) Sketch of a YBCO HEB constriction (of length L, width w, and thickness θ) connected to the arms of a THz planar antenna.

2. Models and Methods

2.1. Describing the Superconducting Transition at THz Frequencies

To have access to the resistance (and, more generally, the impedance) vs. electron temperature T_e of the YBCO constriction at angular frequency $\omega = 2\pi f$, we describe the superconductor by a two-fluid (2F) model. The concentrations of the superconducting and normal charge carriers are n_S and n_N, respectively, with $n_S + n_N = n$, the total free electron concentration [28]. Defining the two-fluid critical temperature ${T_C}^{2F}$, the dependence of $n_N/n = f_N(t_r)$ as a function of reduced temperature $t_r = T_e/{T_C}^{2F}$ was chosen as $f_N(t_r) = {t_r}^4$. This choice minimizes the electron system free energy, according to the Gorter-Casimir 2F model [28]. Hence the real and imaginary parts of the complex conductivity $\sigma = \sigma_1 - j\sigma_2$, assuming Ohm's law is still valid in an impurity scattering description [29]:

$$t_r < 1 : \sigma_1 = \sigma_N t_r^4 + \frac{\sigma_2}{r}, \sigma_2 = \frac{1}{\omega \mu_0 \lambda_0^2} \frac{r^2}{1+r^2}\left(1 - t_r^4\right), \tag{1a}$$

$$t_r \geq 1 : \sigma_1 = \sigma_N, \sigma_2 = 0, \tag{1b}$$

where σ_N is the normal state conductivity, $r = \omega\tau_S$ is the impurity scattering parameter (for scattering time τ_S), μ_0 is the permeability of a vacuum and λ_0 is the London's penetration depth at $t_r = 0$.

As the two-fluid model depicts a homogeneous superconducting material, we have to describe the experimentally observed broadening of the superconducting transition; such a broadening is related to the film microstructure (e.g., grain boundary weak links). This is performed by introducing a Gaussian distribution of critical temperature values, centered at the mid-transition critical temperature T_{C0}, as discussed in Reference [27], with

$$g = \frac{1}{G_N} \exp\left(-\frac{(T_e - T_{C0})^2}{2(\Delta T_G)^2}\right), \tag{2}$$

where G_N is a normalization coefficient and ΔT_G is the critical temperature standard deviation, to be adjusted to fit the experimental transition.

After having expressed the two-fluid resistivity $\rho^{2F}(\omega) = \rho_1^{2F}(\omega) + j\rho_2^{2F}(\omega) = \sigma^{-1}$, we then fit the experimental DC resistivity transition [30] as a convolution product between ${\rho_1}^{2F}$ $(\omega \to 0)$ and the Gaussian function, so that

$$\rho_1^{exp}(T_e, T_{C0}, \Delta T_G) = \left(\rho_1^{2F}(\omega \to 0) \otimes g\right)(T_e, T_{C0}, \Delta T_G). \tag{3}$$

The so-obtained transition is then approximated by a Fermi-Dirac type function, as more appropriate to further numerical treatments (see below Section 2.2, hypothesis 8).

To obtain the THz dependence, we introduce $\rho^{2F}(\omega)$ in the so-obtained DC transition, and then fit a new Fermi-Dirac-like transition with frequency dependent parameters (mid-transition temperature, transition width and minimum resistivity, as detailed in Section 3.1) [27].

2.2. HEB Master Equations

For an HEB constriction of volume $V_C = L \times w \times \theta$ (Figure 1b), the thermal power balance is governed by the heat diffusion equations for the electron and phonon baths, represented by Equation (4a,b), respectively, as follows:

$$\frac{\delta}{\delta x}\left[V_C \kappa_e \frac{\delta T_e}{\delta x}\right] - V_C C_e \frac{\delta T_e}{\delta t} = \frac{V_C C_e \left(T_e^n - T_p^n\right)}{n \tau_{ep} T_{ec}^{n-1}} - L \frac{\delta P_{J-tot}}{\delta x}, \tag{4a}$$

$$\frac{\delta}{\delta x}\left[V_C \kappa_p \frac{\delta T_p}{\delta x}\right] - V_C C_p \frac{\delta T_p}{\delta t} = \frac{V_C C_p \left(T_p^m - T_0^m\right)}{m \tau_{esc} T_{pc}^{m-1}} - \frac{V_C C_e \left(T_e^n - T_p^n\right)}{n \tau_{ep} T_{ec}^{n-1}}, \tag{4b}$$

where indices e and p pertain to the electrons and phonons of the superconducting film, respectively (Figure 1a). κ_e and κ_p are the corresponding thermal conductivities, C_e and C_p the unit volume specific heats (evaluated at temperatures T_{ec} and T_{pc}, respectively). Integers n and m characterize the thermal exchanges between electrons and phonons and phonons and substrate (at reference temperature T_0), respectively. The source term in Equation (4a) represents the Joule power locally injected in a constriction slice of width δx. This power results from both DC and THz currents flowing along the constriction of cross-sectional area $S_C = w \times \theta$. More specifically, after having dropped the higher order terms:

$$\delta P_{J-tot} \approx \frac{\rho(0, T_e(x))}{S_C} I_0^2 \delta x + \frac{\rho(\omega_{LO}, T_e(x))}{S_C} \times \left[\frac{1}{2} I_{LO}^2 + I_{LO} I_S \cos((\omega_{LO} - \omega_S)t)\right] \delta x. \tag{5}$$

In this equation, I_0 is the DC bias current, I_{LO} (local oscillator) and I_S (signal) are the THz current amplitudes at angular frequencies ω_{LO} and ω_S, respectively. The resistivity functions are deduced as discussed in Section 2.1. It therefore appears that (i) the current components are constant over S_C (see below, hypothesis 2) and (ii) the knowledge of $T_e(x)$ is required; this implies an iterative resolution procedure for the coupled Equation (4a,b).

The hypotheses governing the resolution of Equation (4a,b) are given in the following list.

1. These equations obviously describe a phonon cooling mechanism for the electrons in YBCO, as opposed to Nb HEBs, where cooling by electron diffusion to the metal contacts is the dominant process [3,31]. In fact, using YBCO data (cf. Section 3.2, Table 1), we evaluate the electron diffusion length $l_e \approx \pi(\tau_{ep}\kappa_e/C_e)^{1/2} \cong 25$ nm, a significantly smaller value than the constriction length (100 to 400 nm) considered here, so that phonon cooling will prevail [22].
2. It also appears from Equation (5) that the DC and THz current densities are assumed to be constant across the area S_C, a point discussed at length in Reference [32]. Due to the resistivity vs. $T_e(x)$ dependence, DC and THz powers are non-uniformly absorbed along the constriction, as noticed in Reference [33].
3. The constriction ends (at coordinates $x = 0$ and $x = L$) are at reference temperature T_0, which is the cryostat/cryogenerator cold finger temperature (gold antenna contacts). So that: $T_e(0) = T_p(0) = T_e(L) = T_p(L) = T_0$.
4. The solutions $T_e(x)$ and $T_p(x)$ follow the geometrical symmetry of the constriction with respect to its center: $T_e(x) = T_e(L - x)$ and $T_p(x) = T_p(L - x)$. Consequently, the equation solving will be performed in a half-constriction, e.g., $x \in [L/2, L]$.
5. The dissipated power in the constriction tends to raise $T_e(x)$ and $T_p(x)$, which will reach their maximum values at the constriction center, so that: $T_e{}^{max} = T_e(L/2)$, and $T_p{}^{max} = T_p(L/2)$, with $dT_e(L/2)/dx = dT_p(L/2)/dx = 0$.
6. The energy exchange exponent $n = 3$ was taken for YBCO, as extracted from electron-phonon interaction time measurements (see, e.g., Reference [1]). The YBCO to substrate phonon mismatch index $m = 3$ resulted from the number of available phonon modes, proportional to T^3 (Debye's model).
7. The YBCO to MgO substrate phonon escape time was deduced as τ_{esc} (ps) = 75 × θ (nm) [17]. In the case of PBCO/YBCO/PBCO trilayer constriction [30], where PBCO lies for $PrBa_2Cu_3O_{7-y}$, a correction should be applied to θ, as considered in Reference [13].
8. For numerical computation convenience, the resistive superconductive transition has been approximated by a Fermi-Dirac function of the form $\rho = \rho_0\ [1 + \exp((T_C - T_e)/\Delta T)]^{-1}$, to fit the variation given by Equation (3).

9. Due to thermal effects, T_C is sensitive to the constriction DC bias current I_{DC}; this effect has been taken into account by writing $T_C(I_{DC}) = T_C(0)[1 - (I_{DC}/(J^{ref}S_C))^{2/3}]$, where J^{ref} is a reference current density. This point is mentioned in Reference [25] and discussed in Reference [34], in the context of YBCO thin film electrical transport vs. microstructure relationship.
10. Because we can have access to the constriction RF impedance, it was possible to handle the effective power dissipated in the constriction as $\alpha \times P_{LO}$, with $\alpha = \alpha_{imp} \times \alpha'$, where α_{imp} is the impedance matching factor between the constriction and the antenna, and α' represents all the losses from other origins (focusing optics, diplexer, etc.).

2.3. Solving HEB Master Equations

In the two aforementioned Equation (4a,b), we set certain parameter values to limit to two the number of variables to find by the iterative solving method. The known parameters are V_C, κ_e, C_e, n, τ_{ep}, α', S_C, κ_p, C_p, m, τ_{esc}. Formally, the fixed (input) variables are P_{LO}, I_0 and T_0, because in a measurement procedure, these are the parameters controlled by the operator. The resolution of the equations should therefore be performed on the (output) variables $T_e(x)$ and $T_p(x)$, and their second derivatives d^2T_e/dx^2 and d^2T_p/dx^2 as well.

All the above considerations give enough information that the second derivatives can be deduced at each point by our program when x varies from $L/2$ to L. Similarly, $T_e(x)$ and $T_p(x)$ are deduced at each point provided that we define ${T_e}^{max}$ and ${T_p}^{max}$, where the relation ${T_e}^{max} \geq {T_p}^{max}$ will help us to converge. The basic resolution approach is therefore to test (${T_e}^{max}$, ${T_p}^{max}$) pairs until the value found at the extremity of the constriction is: $T_e(L) = T_p(L) = T_0$, which represents our criterion of success for the calculation.

Furthermore, we have made a significant improvement of this basic resolution process, by exchanging the roles of ${T_e}^{max}$ and I_0, such that ${T_e}^{max}$ is now a fixed parameter and I_0 a computational variable. This "trick" facilitates the calculations, because, on the one hand, the ${T_p}^{max}$ solution search is carried out with a fixed upper bound (${T_e}^{max}$ is known). On the other hand, difficult cases where different constriction resistance (R) values can be associated with the same I_0 value (because I_0 is surjective towards R), can be simplified: In fact, ${T_e}^{max}$ is strongly correlated with the resistance (because ${T_e}^{max}$ is bijective with R in all our calculations).

Unlike the formal procedure just described, Equation (5) indicates that I_{LO} (and not P_{LO}) is the THz input, P_{LO} being deduced at the end of the calculation. Therefore, it is not possible to perform a calculation that will accurately give a result ascribed to a given P_{LO} value. What we obtained by our method was a "cloud of points" where each of these points is a configuration of the HEB operating at a certain power P_{LO}, at a certain bias current I_0 and having a certain resistance R (as well as all the other characteristics that we wish to deduce).

The goal of our approach is to obtain a "cloud of points" as homogeneous as possible, in order to extrapolate the operating configurations we are interested in. Typically, we recreated, by interpolation, a series of points that are the I-V responses to the different P_{LO} values we wished to investigate (e.g., $P_{LO} \in [0, 50\ \mu W]$). With these new series of points, we were able to reuse the processing tools for the calculation of the conversion gain and the noise temperature, as further commented in Section 2.4.

The global solving loop process is summarized as follows. Starting with Equation (5), the local heat power dissipation leads to the global heterodyne power mixing expression:

$$P_{J-tot} \approx P_{DC} + \alpha P_{LO} + 2\alpha\left[\sqrt{P_{LO}P_S}\cos((\omega_{LO} - \omega_S)t)\right], \quad (6)$$

where appears the intermediate frequency (IF) $\omega_{IF} = |\omega_{LO} - \omega_S|$. As I_{LO} is homogeneous along the constriction, the RF heat dissipation αP_{LO} is then deduced from the $Z_{RF} = R_{RF} + jX_{RF}$ THz impedance. The result is then fed back into Equation (5), according to:

$$I_{LO} = \sqrt{\frac{2\alpha P_{LO}}{R_{RF}}}, \tag{7}$$

the constriction resistance/reactance contributions being

$$R_{DC} = \int_0^L \frac{\rho(0, T_e(x))}{S_C} dx, R_{RF} = \int_0^L \frac{\rho_1(\omega_{LO}, T_e(x))}{S_C} dx, \text{and} X_{RF} = \int_0^L \frac{\rho_2(\omega_{LO}, T_e(x))}{S_C} dx. \tag{8}$$

It should be noticed that in Equation (7), $\alpha = \alpha_{imp} \times \alpha'$ (hypothesis 10 above) is a function of Z_{RF}, through the impedance matching coefficient

$$\alpha_{imp} = \left(1 - \left|\frac{Z_{RF} - Z_a^*}{Z_{RF} + Z_a}\right|^2\right) \times \frac{\mathrm{Re}(Z_{RF})}{|Z_{RF}|}, \tag{9}$$

where Z_a is the antenna impedance. The left hand term is the regular impedance matching expression, whereas the right hand term is a correction ratio between the RF power dissipated in the constriction and the total input power.

For a self-complementary antenna, $Z_a = R_a + jX_a$ is purely real, with

$$Z_a = R_a = \frac{60\pi}{\sqrt{(1 + \varepsilon_r)/2}}, \tag{10}$$

where ε_r is the substrate material dielectric constant [35,36].

2.4. HEB Mixer Performance

2.4.1. General Considerations and Conversion Gain

For the calculation of the mixer conversion gain and noise temperature, it is necessary to discriminate between: (i) The contribution originating from the DC bias power P_{DC}, and (ii) the contribution originating from the RF power (P_{LO} and P_S). To do this, we first define two parameters K_{DC} and K_{RF} as:

$$K_{DC} = \frac{\delta R}{\delta P_{DC}}(\delta P_{LO} = 0), \tag{11a}$$

$$K_{RF} = \frac{\delta R}{\delta P_{LO}}(\delta P_{DC} = 0), \tag{11b}$$

where R is the constriction resistance (evaluated according to the adopted model), and assuming $P_S << P_{LO}$.

K_{DC} can be deduced from the device $I-V$ relationship at given P_{LO}, whereas K_{RF} cannot be deduced directly. Indeed, the bolometer electrothermal feedback implies that a P_{LO} variation introduces a variation of R, and thus a change of the dissipated P_{DC}. This feedback, which involves power variations ΔP_{DC} and ΔP_{LO}, can be taken into account in K_{RF} from the resistance variation

$$\Delta R = \Delta P_{LO} K_{RF} + \Delta P_{DC} K_{DC}, \text{whence} K_{RF} = \frac{\Delta R}{\Delta P_{LO}} - K_{DC} \frac{\Delta P_{DC}}{\Delta P_{LO}}. \tag{12}$$

The expression of the conversion gain G = (IF power delivered to the load R_L)/(incident RF signal power) = P_L/P_S can be deduced from the small signal IF current $\widetilde{I}$, as (see, e.g., Reference [24]):

$$G = \frac{R_L \widetilde{I}^2/2}{P_S} = \frac{2I_0^2 R_L K_{RF}^2 P_{LO}}{(R_0 + R_L)^2 \left[1 - \frac{K_{DC} I_0^2 (R_L - R_0)}{(R_L + R_0)}\right]^2} \tag{13}$$

where $R_0 = R - \Delta R$ and I_0 is the constriction current when $P_S = 0$.

It is to be noticed that the gain is also involved in the noise expression. Let us consider the noise measured at the mixer input (index "in") and the noise measured at the mixer output (index "out"); the corresponding relationship for the noise temperatures is $T^{in} = T^{out}/G$.

2.4.2. Noise Temperature Contributions

The two main noise contributions of internal origin in a superconducting HEB are the Johnson (Jn) noise and the thermal fluctuation (TF) noise [3,37].

Johnson noise is considered as an additional voltage source v_{Jn} in series with the bolometer, such that $\left\langle v_{Jn}^2 \right\rangle = 4k_B T_0 R_0 \Delta f$, where Δf is the output signal bandwidth. In this context, v_{Jn} introduces variations ΔR_{Jn} and $\widetilde{I}_{Jn}$, hence the noise power $P_{Jn}^{out} = k_B T_{Jn}^{out} \Delta f$ dissipated in the mixer load resistance R_L. Using the conversion gain expression (Equation (13)), one readily obtains the dual sideband (DSB) expression of the mixer input Johnson noise:

$$T_{Jn,DSB}^{in} = \frac{R_0 T_0}{I_0^2 K_{RF} P_{LO}}. \tag{14}$$

The noise spectral density originating from thermal fluctuations of the electrons involves the electron-electron interaction time τ_{ee} and is expressed as follows [24]:

$$\langle T_e \rangle = \sqrt{\frac{4k_B T_e^2 \tau_{ee}}{C_e V_C}}. \tag{15}$$

A current $\widetilde{I}_{TF}$ results from these fluctuations hence the noise power $P_{TF}^{out} = k_B T_{TF}^{out} \Delta f$ dissipated in the load resistance R_L. In the same manner as previously, one obtains the DSB expression of the mixer input thermal fluctuation noise:

$$T_{TF,DSB}^{in} = \frac{1}{K_{RF}^2 P_{LO}} \left(\frac{dR}{dT_e}\right)^2 \frac{T_e^2}{C_e V_C} \tau_{ee}. \tag{16}$$

The global expression of the mixer noise temperature is therefore

$$T_{N,DSB}^{in} = T_{Jn,DSB}^{in} + T_{TF,DSB}^{in} + \frac{T_{IF}}{2G}, \tag{17}$$

where we have introduced the IF amplifier output noise temperature T_{IF}, hence the approximate expression $T_{IF}/2G$ for the DSB input noise temperature. Besides, we have considered here T_{IF} as independent of the working frequency and equal to the cooling temperature T_0 of the HEB [38].

In practice, the mixer performance can be accessed by widespread techniques, such as the Y-factor method [39], which consists in using a blackbody (BB) source alternately adjusted at temperatures $T_{BB} = T_{hot}$ or T_{cold}, and placed at the mixer input. Defining $Y = (P_{hot}/P_{cold})^{out}$ as the ratio between the associated mixer output powers (in the mixer bandwidth Δf), one obtains for the mixer input noise $T_N{}^{in} = (T_{hot} - YT_{cold})/(Y - 1)$ in the Rayleigh-Jeans limit [39]. Moreover, the mixer gain is equal to the slope of the P^{out} vs. $k_B T_{BB} \Delta f$ straight line plot (k_B is the Boltzmann constant).

2.5. Standoff Detection Implementation with an HEB Heterodyne Detector

Passive imaging techniques rely both on collecting naturally emitting radiation from a scene and detecting the contrast between warmer and colder targets. The human being exhibits an emissivity of about 95% at frequencies above 600 GHz, which makes such a target appear warm relatively to a metal object of low emissivity.

We have checked the feasibility of standoff target detection operating in the passive mode with a YBCO HEB THz mixer. We have considered the simplified schematic in Figure 2, which illustrates losses of various origins. The noise equivalent power (*NEP*) requirement for the detector was deduced from the blackbody power P_{BB} emitted by a target of area A_{T} and collected by a detector of area A_{D} (the HEB focusing lens effective area). For a receiver of bandwidth $2\Delta\nu$ at center frequency ν_0 and for a temperature difference ΔT to be resolved at T_{op}, the power difference is

$$\Delta P_{\mathrm{BB}}(\Delta\nu, \Delta T) = \int_{\nu_0-\Delta\nu}^{\nu_0+\Delta\nu} \left[B_\nu(T_{op}+\Delta T) - B_\nu(T_{op})\right] \mathrm{d}\nu \varepsilon_{\mathrm{T}} \frac{A_{\mathrm{D}} A_{\mathrm{T}}}{d_{\mathrm{T}}^2}, \tag{18}$$

where $B_\nu(T)$ is the blackbody spectral radiance (in $\mathrm{W{\cdot}m^{-2}{\cdot}sr^{-1}{\cdot}Hz^{-1}}$), ε_{T} the target emissivity, and d_{T} the target to detector distance (possibly corrected to include imaging system primary and secondary mirrors).

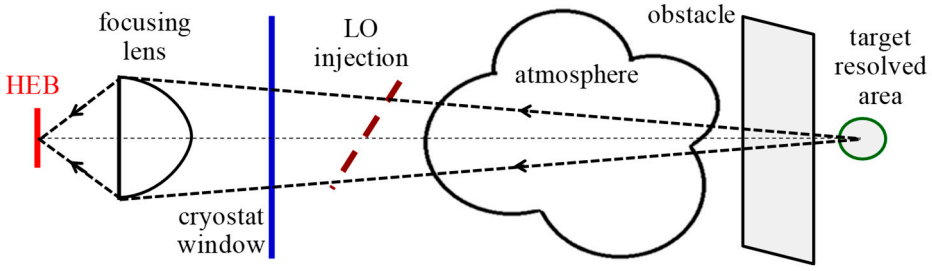

Figure 2. Simplified schematic for HEB standoff THz detection arrangement. The target resolved area is deduced from the Airy pattern at the HEB location (Equation (19)).

The *NEP* was then obtained by assuming the resolution to be diffraction limited for the detector (i.e., at the focusing lens focal plane). Consequently, the resolved distance at the target can be related to the Airy disk diameter at the detector focal plane by a factor $d_{\mathrm{T}}/f_{\mathrm{L}}$, approximately, where f_{L} is the focal length of the focusing lens. We finally work out at wavelength λ:

$$NEP = \frac{\int_{\nu_0-\Delta\nu}^{\nu_0+\Delta\nu} \left[B_\nu(T_{op}+\Delta T) - B_\nu(T_{op})\right] \mathrm{d}\nu}{\sqrt{\delta\nu_{\mathrm{int}}}} \varepsilon_{\mathrm{T}} \left(\frac{\pi 1.22\lambda}{2}\right)^2 t_{\mathrm{opt}} t_{\mathrm{atm}} t_{\mathrm{obs}}, \tag{19}$$

where $\delta\nu_{\mathrm{int}} = 1/(2\pi\tau_{\mathrm{int}})$, τ_{int} being the (e.g., post-detection) integration time; t_{opt}, t_{atm}, and t_{obs} are the transmission factors related to optics, atmosphere and obstacles, respectively (Figure 2). These factors are considered in the following.

- t_{opt} includes the HEB planar antenna main lobe efficiency, the focusing lens and the detector cryostat window losses, and the LO injection losses (diplexer or beam splitter).
- t_{atm} was extracted from the atmospheric attenuation factor α_{atm} (in dB/m) in various conditions, using the Atmospheric Effects Model (AEM) described in Reference [40]. Such extracted values were also in line with values deduced from data in Reference [41].
- t_{obs} represents the transmission through some obstacle existing in front of the target (cloth, cardboard, etc.).

The double sideband noise temperature required for the HEB was deduced from the *NEP* in the Rayleigh-Jeans limit as [39]:

$$T_{\mathrm{DSB}} = \frac{NEP}{2k_B\sqrt{2\Delta\nu}}. \tag{20}$$

3. Simulation Results

3.1. YBCO Superconducting Transition in the THz Range

As shown in Section 2.3, we have been able to link the experimental DC transition with a two-fluid model representation of the resistive transition when $\omega \to 0$. From this result, we perform at terahertz frequencies a similar convolution as in Equation (3), which will therefore modify the modeled resistive transition accordingly. We approach this modification as the combination of three phenomena: The decrease of the average mid-transition critical temperature (T_C), the widening of the resistive transition (ΔT) and the appearance of a minimum resistivity (ρ_{min}). To the first order, we write:

$$T_C(f_{\mathrm{THz}}) = T_C(0) \times (1 - A_T f_{\mathrm{THz}}), \tag{21a}$$

$$\Delta T(f_{\mathrm{THz}}) = \Delta T(0) \times (1 + B_T f_{\mathrm{THz}}), \tag{21b}$$

$$\rho_{\mathrm{min}}(f_{\mathrm{THz}}, t_r = 0.8) \cong 2\rho_{\mathrm{min}}(f_{\mathrm{THz}}, t_r = 0) = C_T f_{\mathrm{THz}}. \tag{21c}$$

In practice, the A_T, B_T and C_T parameters are introduced in the expression of the resistivity according to a Fermi-Dirac function (for convenience in our simulation). Their values are calculated for a given material and approximated for the 0 to 5 THz frequency range. Thus, in a first step, it is necessary to calculate C_T from the expression of ρ_{min} deduced from $\rho^{2F}(\omega, t_r \to 0)$, as presented in Equation (21c). The pair of parameters (A_T, B_T) is then calculated by determining the pair which minimizes the difference function between the gaussian fit and the current resistivity function $|\rho_G(T, \omega) - \rho(T, \omega)|$, in both the 50 to 100 K and 0 to 5 THz ranges.

From an experimental point of view, our current technological process allows to achieve YBCO constrictions of length and width $L = w = 400$ nm and thickness $\theta = 35$ nm, with a mid-transition critical temperature $T_C = 89$ K [25,30], a transition width of 1.2 K and a conductivity $\sigma_N = 3.15 \times 10^5\ \Omega^{-1}\cdot m^{-1}$. Such constrictions were made from YBCO films sputtered on MgO (001) single crystalline substrates. X-ray diffraction confirmed the mainly *c*-axis orientation of the films, with rocking curves exhibiting full width at half maximum values of ~ 0.18 degree for the (005) YBCO line. Weak parasitic lines were observed however, which indexation could also confirm the presence of *a*-axis growth [16]. The measured *c*-axis lattice parameter values ranged from 1.169 to 1.170 nm, which are close to the value of fully oxygenated $Y_1Ba_2Cu_3O_7$ films [42]. Besides, in-plane twinning of the films is expected [43]. The film surface morphology was uniform with a typical roughness of about 4.5 nm rms independent of the YBCO thickness [44].

For a YBCO constriction exhibiting such dimensions, our simulation results lead to: $A_T = 0.011\ \mathrm{THz}^{-1}$, $B_T = 0.186\ \mathrm{THz}^{-1}$ and $C_T = 6.82 \times 10^{-8}\ \Omega\cdot m\cdot \mathrm{THz}^{-1}$. Those results are illustrated in Figure 3.

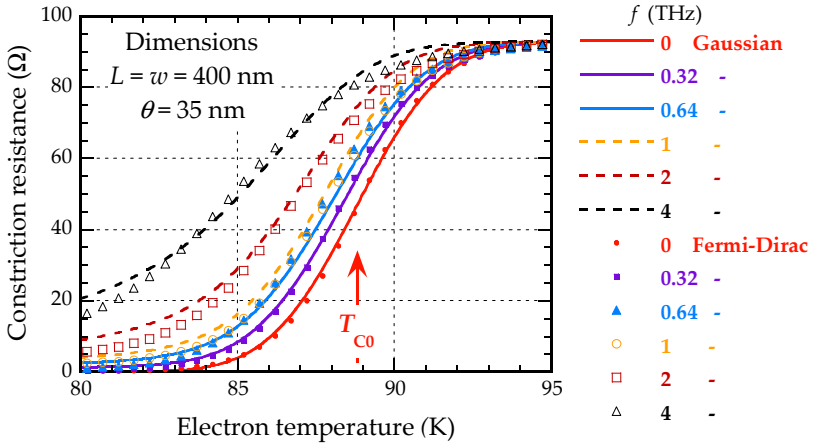

Figure 3. Frequency-dependent YBCO superconducting transition illustrated by the constriction resistance vs. frequency. The DC plot (f = 0) is a fit from experiment [30]. The gaussian curves describe the T_C distribution as discussed in the text. Fermi-Dirac fits have been used for the device performance simulation as more appropriate to the convergence of numerical solutions. Redrawn after [27].

3.2. DC Characteristics

For our simulations, we have considered two HEB devices (data gathered in Table 1). The constriction dimensions of device A are close to the limits achievable with e-beam lithography; these dimensions are those considered in the "0D" HEB model [22]. The constriction dimensions of device B are those achievable with our currently available technological process, combining optical and e-beam lithography [25]. Device B is also the constriction example taken in Section 3.1.

3.2.1. Temperature Profiles

The temperature profiles (solutions of Equation (4a,b)), shown in Figure 4 for devices A and B exhibit features, typically representing the HEB phenomena, namely: (i) The hot electron condition $T_e(x) > T_p(x)$, and (ii) the hot spot (i.e., normal state) region Δx^{HS} such that $T_e(x) > T_C$ for $x \in \Delta x^{HS}$. We notice that $T_e(x)$ is closer to $T_p(x)$ for device B; this is due to the stronger phonon film to substrate escape efficiency, as testified by the ~3.5 times longer τ_{esc} value for device B (Table 1).

Table 1. For constrictions A and B, device characteristics and YBCO physical parameters used in the simulations. Unless otherwise stated, the parameter values are those of [22].

Device	L, w (nm)	θ (nm)	C_e (J·m^{-3}·K^{-1})	C_p (J·m^{-3}·K^{-1})	κ_e (W·m^{-1}·K^{-1})	κ_p (W·m^{-1}·K^{-1})	
A	100	10	2.5×10^4	6.5×10^5	1	10	
B	400	35	2.5×10^4	6.5×10^5	1	10	
Device	τ_{ep} (ps)	τ_{esc} (ns)	σ_N [1] (Ω^{-1}·m^{-1})	J_C [2] (A·cm^{-2})	T_C [3] (K)	ΔT (K)	T_0 (K)
A	1.0	0.75	3.15×10^5	2.2×10^6	85	1.2	60
B	1.7	2.6	3.15×10^5	2.2×10^6	89	1.2	70

[1] Normal state conductivity at ~ 100 K. [2] Critical current density at 77 K. [3] Mid-transition critical temperature.

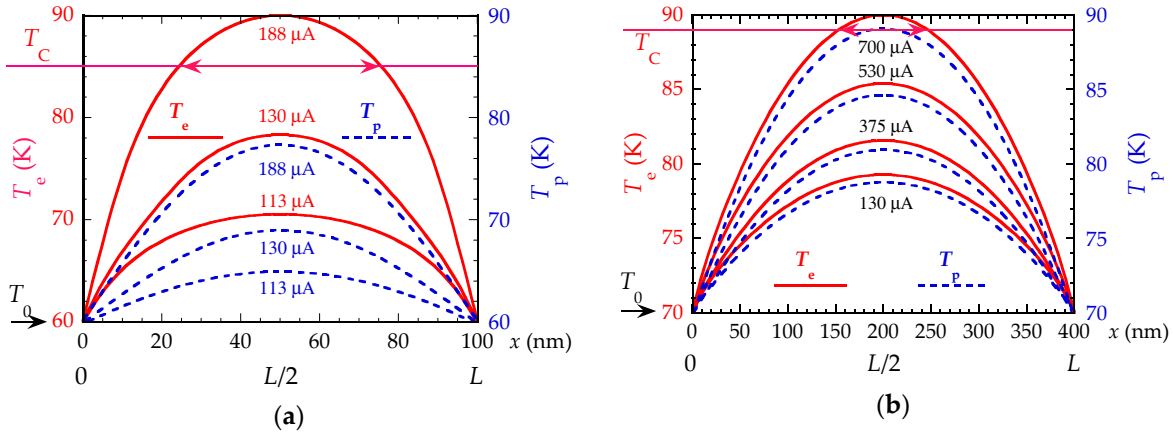

Figure 4. For devices A and B, electron temperature $T_e(x)$ (solid curves) and phonon temperature $T_p(x)$ (dashed curves) profiles: (**a**) For device A (P_{LO} = 5 µW); (**b**) for device B (P_{LO} = 35 µW). T_0 and T_C are the reference (cold finger) and mid-transition critical temperatures, respectively. Arrows on T_C lines delimit the hot spot regions Δx^{HS} (see text). Curve labels indicate the DC bias current I_0 values.

As a check of the validity of our simulation approach, we run our procedure with low-T_C material data for the NbN constriction considered in Reference [24]. We obtained $T_e(x)$ profiles very close to each other (less than 5% difference). This was verified for various P_{LO} values in the quasi-static (QS) regime, i.e., at the low ω_{LO} frequency limit of the constriction impedance (Equation (8)).

3.2.2. Current-Voltage Plots

The $T_e(x)$ profile allows to have access to the resistivity profile along the constriction, hence to the constriction resistance/impedance by integration (Equation (8)). As explained in Section 2.3, the *I-V* plots can then be deduced in the form of "clouds of points". This representation illustrates, in color/gray tone levels, the device DC response as a function of e.g., P_{LO}, as shown in Figure 5 for devices A and B.

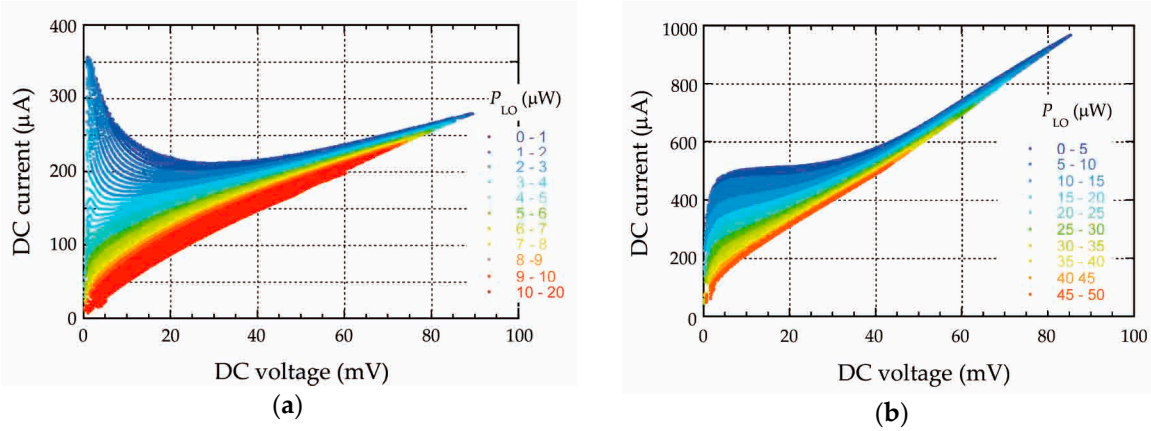

Figure 5. For devices A and B, DC current vs. DC voltage maps according to P_{LO} values, at 400 GHz LO frequency: (**a**) For device A (T_0 = 60 K); (**b**) for device B (T_0 = 70 K). Redrawn after [45].

With regard to device A, we notice that the *I-V* dependence can be hysteretic: For a given bias current value, there are three distinct HEB voltage operating points. Indeed, in the 5 mV to ~ 15 mV range, the differential resistance is negative, this behavior being typical of HEBs operating at low T_0 and exhibiting a short film to substrate escape time. Consequently, the largest voltage variations, as P_{LO} varies, where a larger part of the constriction is still superconducting, are situated below ~ 30 mV. This effect is not observed for device B, due to the longer escape time in that latter case.

For further verification, we also compared, for an NbN device, our *I-V* results with those reported in Reference [24]. As shown in Figure 6, the calculated values are close to the HEB measurements at bias currents above 20 µA. The result of our calculation for P_{LO} = 220 nW is, however, noticeably different from that reported in Reference [24]. This is seemingly due to the difference in the computational method, but this difference does not affect the calculation of the dynamic performances (conversion gain and noise temperature) of the HEB.

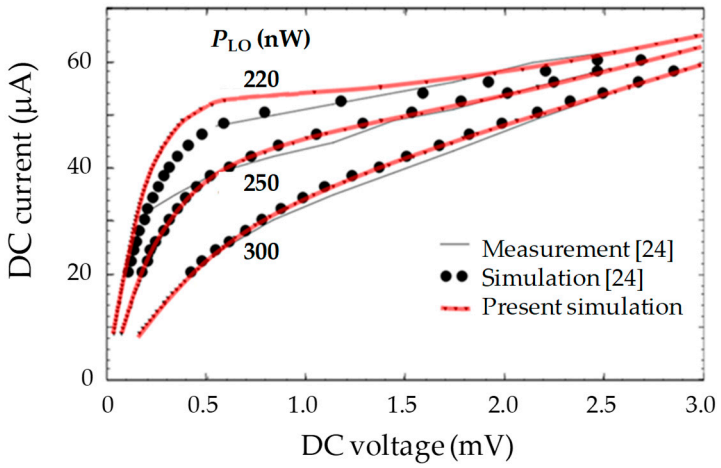

Figure 6. For the NbN HEB reported in Reference [24], the comparison between *I-V* plots measured on the fabricated device and simulation according to the model developed in Reference [24] and our present model.

3.3. Mixer Performance

The noise temperature and the conversion gain were determined at given local oscillator power P_{LO}; they were deduced from the heat equations solving results and presented in the form of "clouds of points" (see Section 2.3). To highlight the influence of P_{LO} for a given DC bias power P_{DC}, we have illustrated those results as P_{DC} vs. P_{LO} maps. We have considered four operating frequencies: The quasi-static (QS) regime, 500 GHz, 2.5 THz and 4 THz. The results are presented in the following.

3.3.1. Noise Temperature

We observe in Figure 7 that the minimum noise P_{DC} vs. P_{LO} area evolves in level and that the optimal P_{LO} value also evolves (see Table 2 below). In particular, we notice that the secondary area of low noise temperature, starting at $P_{LO} \approx 35$ µW in the QS mode, vanishes when the frequency increases.

Table 2. For an HEB of dimensions $L = w = 400$ nm and $\theta = 35$ nm at different operating frequencies, with matching coefficient α_{imp} included, compared performances at an optimal operating point with respect to the noise temperature.

Frequency	I_{DC} (µA)	R (Ω) [1]	P_{DC} (µW)	P_{LO} (µW)	G (dB)	T_{DSB} (K)
QS	454	21.3	4.4	7.5	−9.0	1781
500 GHz	464	21.4	4.6	7.5	−7.1	1208
2.5 THz	394	14.6	2.3	12.5	−6.1	1013
4 THz	379	13.0	1.9	13.5	−6.5	1093

[1] RF resistance.

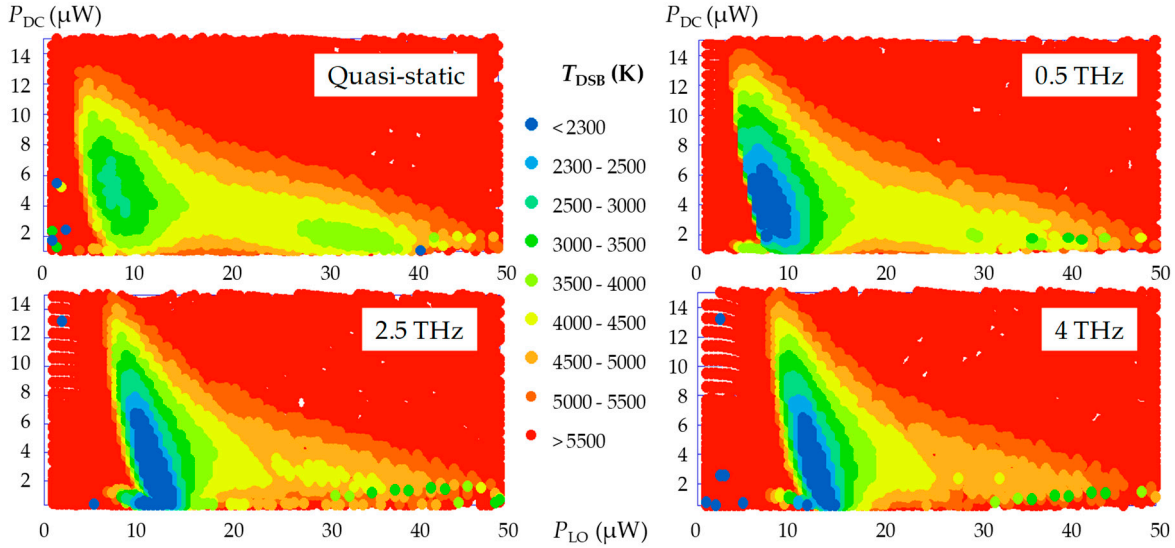

Figure 7. For an HEB constriction of dimensions $L = w = 400$ nm and $\theta = 35$ nm (Figure 1), maps exhibiting double sideband noise temperature T_{DSB} levels in DC bias power vs. LO power coordinates. Impedance matching coefficient α_{imp} with the antenna was included.

This consideration can be furthered by separating the sources of noise for the two cases of QS regime and LO frequency at 2.5 THz (Figure 8). The contribution of each noise source informs us about the evolution of the area where the noise is minimum. We notice that in the QS regime, the fluctuation noise is minimal when $P_{LO} > 20$ μW, whereas at 2.5 THz the low noise area is distributed differently, with improved noise level when 10 μW < P_{LO} < 15 μW.

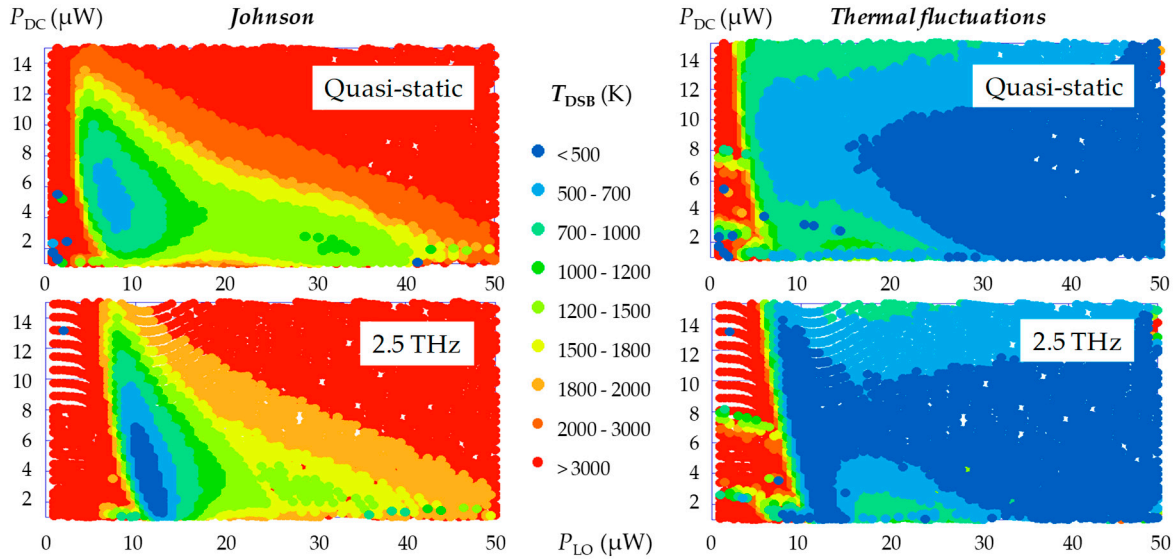

Figure 8. For an HEB constriction of dimensions $L = w = 400$ nm and $\theta = 35$ nm (Figure 1), maps exhibiting Johnson noise and thermal fluctuation noise contributions to T_{DSB} levels in DC bias power vs. LO power coordinates. Impedance matching coefficient α_{imp} with the antenna was included.

3.3.2. Conversion Gain and Summary of Mixer Results

We then resume the comparison for the conversion gain at the four working frequencies, as shown below in Figure 9. The gain decreases as P_{DC} increases, and is maximized at given P_{LO}. Thus, as the frequency of the local oscillator increases, the conversion gain appears to be maximum around 2.5 THz and requires a local oscillator power of 12.5 μW (see Table 2 below).

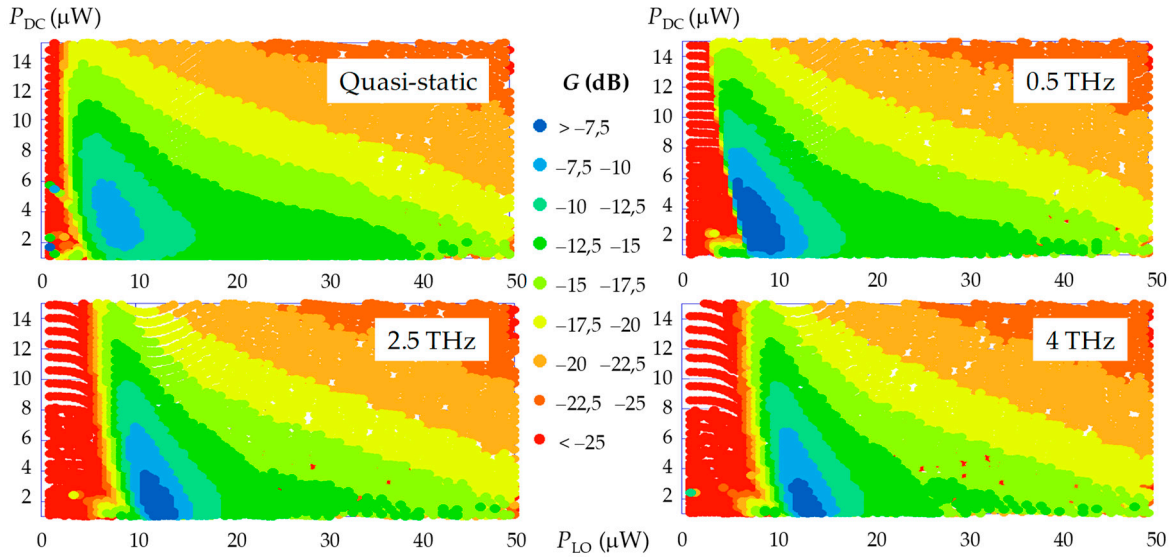

Figure 9. For an HEB constriction of dimensions $L = w = 400$ nm and $\theta = 35$ nm (Figure 1), maps exhibiting G levels in DC bias power vs. LO power coordinates. Impedance matching coefficient α_{imp} with the antenna was included.

As compared to previous results [25], the present model highlights a sharp decrease in the local oscillator power needed to operate the HEB at the optimum point. Intuitively, one might be inclined to think that after taking into account α_{imp} coupling losses, P_{LO} should increase as $1/\alpha_{imp}$. In fact, the present model introduces two physical properties, namely the influence of the non-uniform distribution of the dissipated LO power, and the impedance matching coefficient between the antenna and the nano-constriction, which alter the response of the simulated HEB.

Indeed, the dissipation of the radiofrequency current is concentrated in the resistive zone of the nano-constriction, where dominates the dissipation by Joule effect (hot spot). Thus, if for example a quarter of the nano-constriction is resistive, then the power will be mainly dissipated in this zone, thus reducing a prerequisite of 35 μW (calculated in the model of the "regular" hot spot adapted to YBCO [25]) down to 7.5 μW.

3.3.3. IF Bandwidth

Small signal analysis (as formulated in Reference [25]) was performed to determine the IF response in terms of conversion gain as a function of the intermediate frequency $f_{IF} = (\omega_{LO} - \omega_S)/2\pi$, as originating from the last term in Equation (5). This is illustrated in Figure 10 for devices A and B. The main features are: (i) The low frequency regular bolometric response plateau, (ii) the regular bolometric cutoff associated with the escape time τ_{esc}, (iii) a second plateau characterizing the HEB action, (iv) the HEB cutoff associated to the YBCO intrinsic relaxation time τ_{ep}. Clearly, the bandwidth is limited by the τ_{esc} value (Table 1), which is in favor of ultrathin and small volume constrictions [23,25]. It therefore appears that a bandwidth close to 1 GHz can be expected for device A.

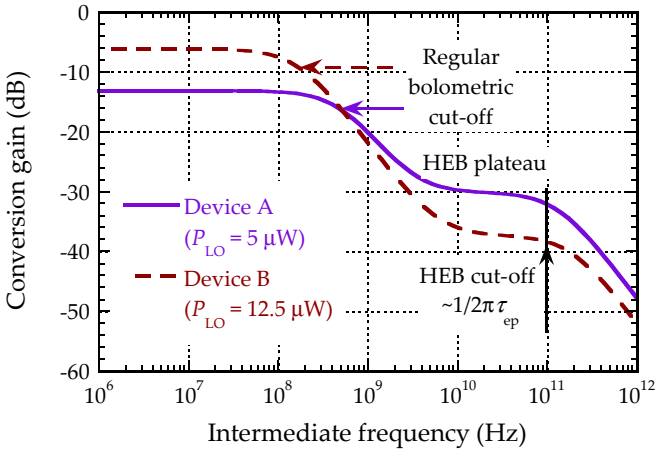

Figure 10. For devices A and B, conversion gain vs. f_{IF}, at P_{LO} values minimizing T_{DSB}. Data for device A were available in the QS regime [25], whereas data at 2.5 THz were used for device B [45].

3.4. Standoff Detection Performances Requirements

We have run the simulation for the standoff system, as presented in Section 2.5 (Equations (18)–(20)), with detector double sideband width $2\Delta\nu$ = 2 GHz and integration bandwidth $\delta\nu_{int}$ = 1 Hz. Five frequencies centered in atmospheric transmission windows were considered: 670 GHz, 1.024 THz, 1.498 THz, 2.522 THz, and 3.436 THz. Besides, the detection scenario was chosen according to the following parameters:

- Target emissivity $\varepsilon_T = 1$.
- Optical losses were evaluated according to the antenna main lobe efficiency (−2 dB), the focusing lens and the detector cryostat window losses (−1 dB), and the LO injection losses (beam splitter: −3 dB), amounting to $t_{opt} \cong 24\%$.
- t_{atm} was determined for various relative humidity values (*RH*, in the 10% to 70% range) at operating temperature T_{op} = 295 K, at sea level and with clear atmospheric conditions (e.g., no dust).
- t_{obs} was calculated for light cotton clothing from data in Reference [46] for frequencies below 1 THz, and in Reference [47] for frequencies above 1 THz. Values of t_{obs} for the five selected frequencies are collected in Table 3.

Table 3. Transmission coefficient through an obstacle of light cotton cloth [46,47].

Frequency (THz)	0.67	1.02	1.49	2.52	3.44
t_{obs} **(%)**	75	47	21	2	0.1

Various values of temperature resolution ΔT were taken into account, from 0.5 K to 10 K, with respect to the results obtained as a function of the pertinent parameters (frequency, target distance).

Figure 11a exhibits the required HEB mixer noise temperature for a passive mode detection system as a function of frequency and atmospheric relative humidity level for a 10 m target distance and a resolution ΔT = 1 K. The influence of relative humidity strongly occurs at frequencies higher than 2.5 THz (for instance, a low value of $T_{DSB} \approx 85$ K is required for a system operating at 2.5 THz at *RH* level of 40 %). In order to reach a viable standoff passive detection operation with T_{DSB} values technologically reachable, it is therefore necessary to reduce either the target distance or the temperature resolution.

Figure 11b exhibits the required noise temperature as a function of target distance and resolution temperature at 2.5 THz and highly stringent *RH* level of 70%. Thus, for instance, at 5 m target distance,

the detection system would require $T_{DSB} \approx 110$ K for $\Delta T = 1$ K, a restrictive parameter which could be relaxed to T_{DSB} approaching 1100 K for $\Delta T = 10$ K.

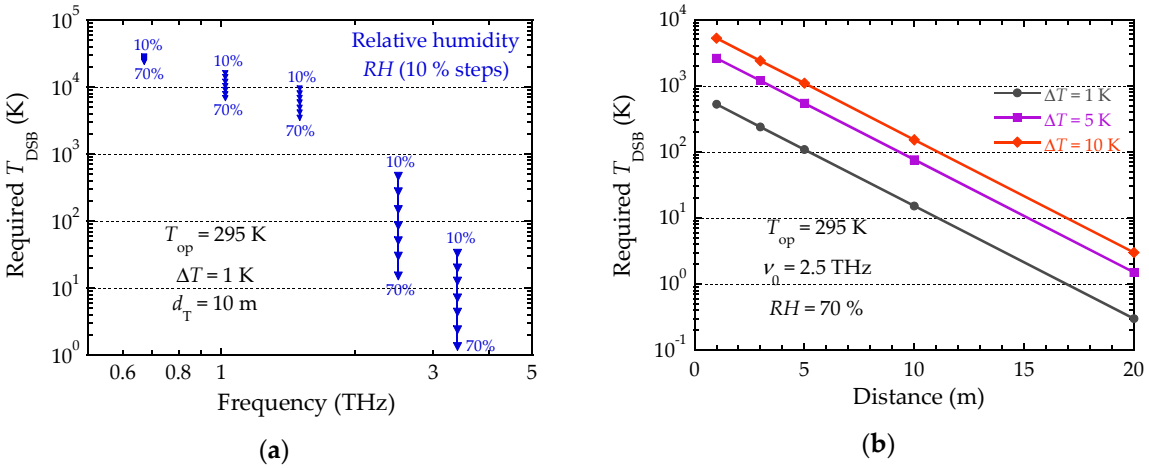

Figure 11. Standoff detection double sideband noise temperature requirements: (**a**) As a function of operating frequency for various atmospheric humidity contents (at fixed ΔT and d_T); (**b**) as a function of target distance for various target temperature resolutions (at fixed ν_0 and RH).

4. Discussion

In this discussion, we focus on a limited number of points specific to our present modeling approach, where it differs from either our previous modeling hypotheses or previously published models. We wish also to compare between our simulations and some experimental results, unfortunately very few in the case of YBCO HEBs.

4.1. Inhomogeneous P_{LO} Hypothesis Effect on I-V Plots at Low DC Voltage

Our model introduces the matching factor α_{imp} between the terahertz antenna and the nano-constriction, of impedance $R_{RF} + jX_{RF}$. This impedance is very small at low P_{DC} and P_{LO} power levels (say < 1 μW). In that case, $\alpha_{imp} \cong 0$ and therefore the contribution of αP_{LO} in the heat equations seems to be negligible: If it were true, the *I-V* plots would be very similar at various P_{LO} levels.

In Figure 12, however, we observe two very different distributions between the *I-V* plots, according to P_{LO} values. The reason is related to the method of calculation, as considered now.

- In the conventional hot spot method (homogeneous P_{LO} dissipation), the LO power expression, including impedance matching, is written as:

$$\alpha P_{LO} = \alpha' \frac{4R_a R}{(R_a + R)^2} P_{LO}, \tag{22}$$

  where R is the constriction resistance, R_a is the antenna resistance, P_{LO} is the power actually applied prior to losses, and is deduced from αP_{LO} which is the power used for the hot spot calculation. When $R \to 0$, $\alpha P_{LO} \to 0$ at all P_{LO} values (Figure 12a).
- In the hot spot method with RF current (inhomogeneous P_{LO} dissipation), the terahertz power is determined from the intensity of the terahertz current, as outlined in Section 2.3 (Equations (6)–(10)). After some manipulations, still with the constriction low impedance value hypothesis, the following I_{LO} vs. P_{LO} relationship can be worked out [27]:

$$I_{LO} \approx \sqrt{\alpha' \frac{8P_{LO}}{R_a\sqrt{1+r^2}}}. \tag{23}$$

Even at low P_{DC} and P_{LO} levels, we observe there is a non-zero $I_{LO} \propto P_{LO}{}^{1/2}$ along the constriction in the superconducting state. If P_{LO} is strong enough, the critical temperature $T_C(I_{LO}) < T_0$ and R_{RF} is no longer negligible. Consequently, the P_{LO} dissipation causes the increase of the electron temperature and therefore a non-zero resistance even at low current (Figure 12b).

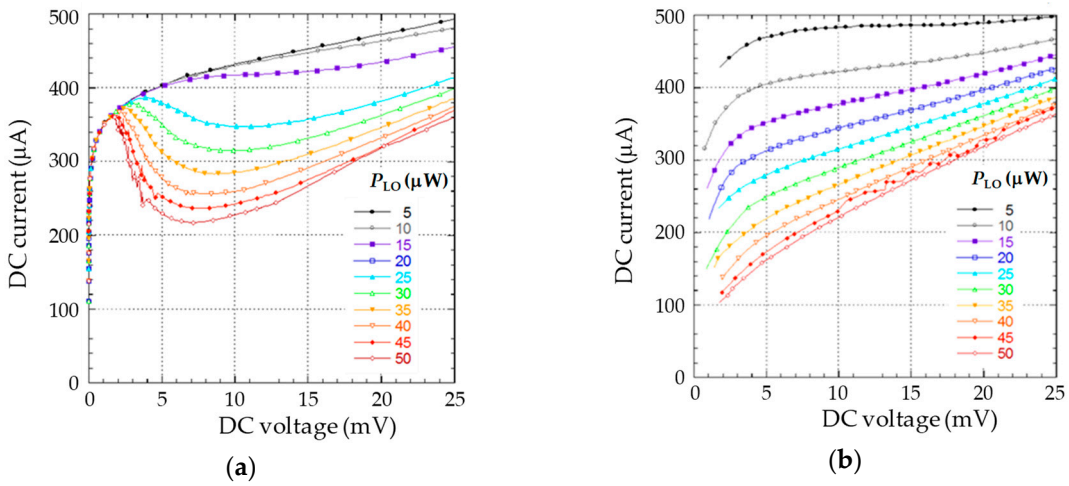

Figure 12. Comparing low-voltage behavior of DC *I-V* plots taking impedance matching factor with antenna into account: (**a**) Regular hot-spot model with uniform P_{LO} power dissipation along the constriction; (**b**) our hot-spot model approach with I_{LO} as an input parameter, i.e., non-uniform P_{LO} power dissipation.

Figure 12a illustrates how impedance matching is not correctly formulated with conventional HEB models, in which powers of both DC and RF origins are confounded. The resulting DC plots (the *I-V* curves seem to be merging) are observed neither in the NbN nor YBCO-based HEB measurements. P_{DC} and $\alpha_{imp}P_{LO}$ are quite distinct in the RF current hot spot model, which makes it possible to obtain results consistent with the typical HEB *I-V* measurements (Figure 12b).

Another verification has been possible through DC *I-V* plots simulated at 650 GHz and compared to measurements performed on a YBCO device ($L = w = 300$ nm, $\theta = 30$ nm) made available to us [48,49], and further considered in Reference [50]. Although not entirely quantitative, the constriction pumping effect by the LO power is clearly visible in Figure 13. We also observe a better similarity between those results and the *I-V* curves in Figure 12b, rather than those in Figure 12a, so in favor of our complete model with RF current.

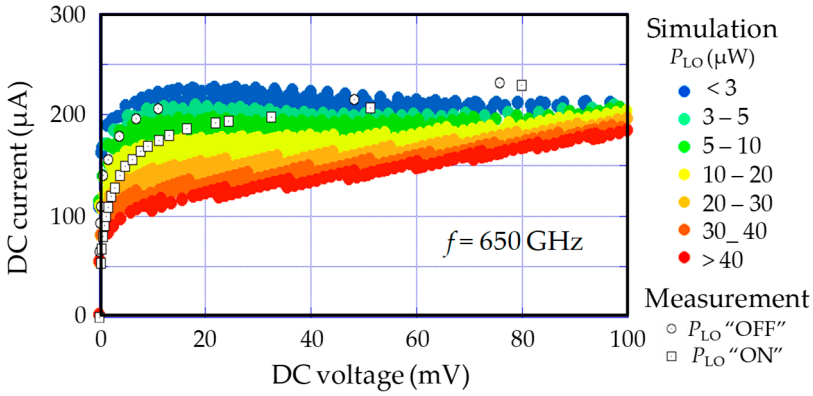

Figure 13. For a YBCO HEB, *I-V* map, with P_{LO} levels, from our simulation with 650 GHz RF current (non-uniform LO power dissipation). Measurement points, without and with LO power applied at the same frequency, are also indicated (courtesy J. Raasch [48]).

4.2. Taking the Resistivity Limit in the Superconducting Transition into Account

The limits of the THz superconducting transition model appear when the normal state resistivity is very high (because YBCO tends to deteriorate with aging [16]); in this case, the effects of the working frequency are of little significance. It is possible to calculate an order of magnitude of this resistivity limit by considering the $\rho^{2F}(\omega,t_r \to 0)/\rho_N > 1\%$ criterion; starting from Equation (1a,b), we can work out:

$$\frac{\rho^{2F}(\omega, t_r \to 0)}{\rho_N} \approx \frac{\omega \mu_0 \lambda_0}{3}. \tag{24a}$$

According to the limit criterion and Equation (21c) we obtain:

$$\frac{\rho^{2F}(f_{THz}, t_r \to 0)}{\rho_N} \approx \frac{f_{THz} \times 1.05 \times 10^{-7}}{\rho_N} > 1\%. \tag{24b}$$

The resistive transition model should therefore be used at frequencies such that $f_{THz} > \rho_N \times 9.5 \times 10^4$, which is the case of our study, where the typical normal state resistivity is $\rho_N = 3.2 \times 10^{-6}$ Ω·m and our calculation frequency $f_{THz} \geq 0.3$ THz.

Besides, it is possible to carry out the calculation further, because our two-fluid dispersive model also makes it possible to express the imaginary part of the resistivity ${\rho_2}^{2F}$ (kinetic inductance effect). A calculation result of the constriction impedance $R_{RF}(T_e) + jX_{RF}(T_e)$ is shown in Figure 14. We notice that the reactive part reaches its maximum near the middle of the resistive transition, where the detectors are considered the most sensitive, because dR_{RF}/dT_e is optimal.

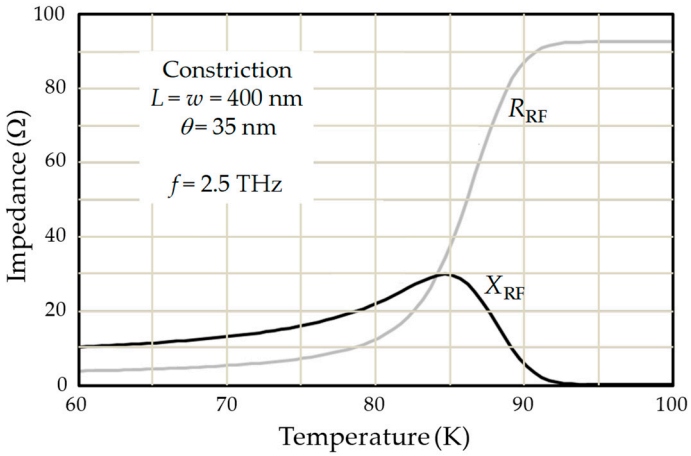

Figure 14. Example of the real and imaginary parts of a total THz impedance of a constriction; the temperature was assumed uniform in this case.

However, there is no obvious function to represent the variations of ${\rho_2}^{2F}(\omega,T_e)$. It is therefore necessary to know the YBCO temperature distribution along the constriction and solve the complete convolution calculation to estimate ${\rho_2}^{2F}$ and to deduce the imaginary part of the constriction impedance. We therefore opted for this procedure as part of the hot spot model as presented above.

4.3. Mixer Noise: Effect of Taking the Impedance Matching Factor into Account

The best operation area at $P_{LO} \approx 10$ μW, as observed in Section 3.3.1, was not present in our previous model without impedance matching [25]; we therefore studied the influence of taking into account the impedance matching factor between the antenna and the nano-constriction on the noise temperature.

As already mentioned, our approach shows that there may be cases where the loss of coupling efficiency, due to impedance mismatch, may increase the sensitivity of the device. This influence is

more evident by considering the distribution of calculated noise temperatures with non-constant α_{imp} (shown previously in Figure 7) and compare it to the distribution of noise temperatures with constant α_{imp} (= 1), as shown below (Figure 15). We notice a significant change in the position of the better operation area. In the quasi-static mode, the best operation area at $P_{LO} \approx 10$ µW is no longer present and, in general, the noise temperatures are higher when the impedance matching is not taken into account (see Table 4).

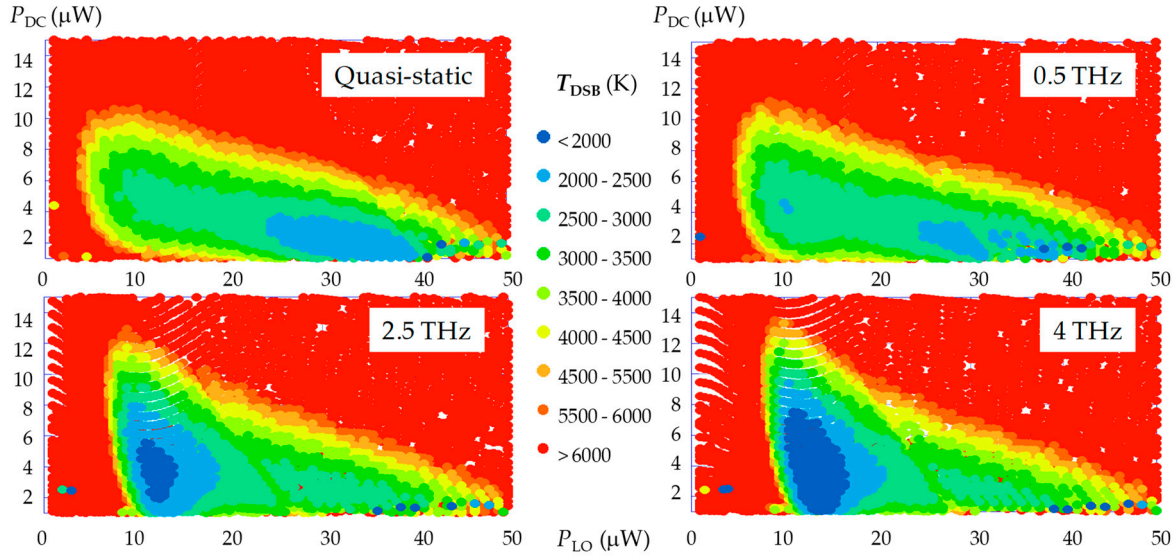

Figure 15. For an HEB constriction of dimensions $L = w = 400$ nm and $\theta = 35$ nm (Figure 1), maps exhibiting double sideband noise temperature T_{DSB} levels in DC bias power vs. LO power coordinates. Impedance matching coefficient with the antenna was not included (α_{imp} = constant = 1).

Table 4. For an HEB of dimensions $L = w = 400$ nm and $\theta = 35$ nm at different operating frequencies, with unit impedance matching coefficient ($\alpha_{imp} = 1$), compared performances at an optimal operating point with respect to the noise temperature.

Frequency	I_{DC} (µA)	R (Ω) [1]	P_{DC} (µW)	P_{LO} (µW)	G (dB)	T_{DSB} (K)
QS	241	27.9	1.6	35	−13.8	2607
500 GHz	271	26.4	1.9	30	−13.6	2704
2.5 THz	392	19.2	3.0	12	−10.8	2332
4 THz	389	18.2	2.7	12.5	−10.1	2021

[1] RF resistance.

In this discussion, where the influence of impedance matching is removed, the noise distribution as a function of frequency is only subject to change according to the distribution of P_{LO} along the nano-constriction. We clearly observe (Table 4): (i) A decrease in the prerequisite of P_{LO}, and (ii) an improvement of the noise temperature when the operating frequency increases. This is due to the influence of the distribution of P_{LO} along the nano-constriction which is in question: This distribution is more localized in the quasi-static regime than at 4 THz, to take the extreme cases.

As part of a model to optimize the manufacturing of future HEBs, this result demonstrates the importance of taking impedance matching into account. The parameters to consider for manufacturing an HEB are the dimensions of the nano-constriction and the quality of the film, but also the resistive characteristic of the antenna, whose appropriate adjustment of the impedance should allow a gain in performance.

4.4. Comparing Simulated Mixer Noise with Experimental Results

A significant number of HEB heterodyne mixer performance experimental results are gathered in Figure 16.

The state-of-the-art HEB mixers are made from epitaxially grown low-T_C superconducting ultrathin films: Nb HEBs mainly below 1 THz, and (100) NbN HEBs above 1.4 THz. For example, values of T_{DSB} = 600 K at 2.5 THz, with a large noise bandwidth in excess of 7 GHz [51], and T_{DSB} = 815 K at 4.7 THz [52] were reported for NbN HEBs. However, T_C values for these HEB devices remain below 11 K. An interesting alternative can be offered with HEBs made from *c*-axis oriented MgB_2 ultrathin films [20,53], due to increased operation temperature (T_C = 39 K) and expected instantaneous bandwidth up to 10 GHz.

We notice the small number of published data concerning YBCO devices. As already mentioned in our introduction, this situation can be attributed to YBCO nanostructuration challenges, therefore a performance degradation associated with aging effects, even on highly *c*-axis oriented YBCO ultrathin films. Among these, the result at 585 GHz reported in Reference [15] concerns a rather large constriction (L = 1 μm, w = 2 μm, θ = 100 nm) exhibiting T_{DSB} = 3600 K and G = − 11 dB at P_{LO} = 1 μW. It may be compared to our performance prediction for a device B (Table 1) under not optimized conditions at 750 GHz (T_{DSB} = 3000 K and G = − 10.8 dB at P_{LO} = 9 μW [27]). Besides, the very large T_{DSB} values reported in Reference [13] were attributed to inadequate experimental conditions by the authors, who predicted an improvement of $T_{DSB} < 10^4$ K up to 6 THz (system noise temperature), a figure compatible with our predicted $T_{DSB} = 5 \times 10^3$ K (mixer noise temperature, not optimized [27]) at 2.5 THz. Our present optimized predictions (solid curve in Figure 16) have therefore to be taken as a limit that could be reached with improved nano-structuring of *c*-axis oriented YBCO ultrathin films [54,55].

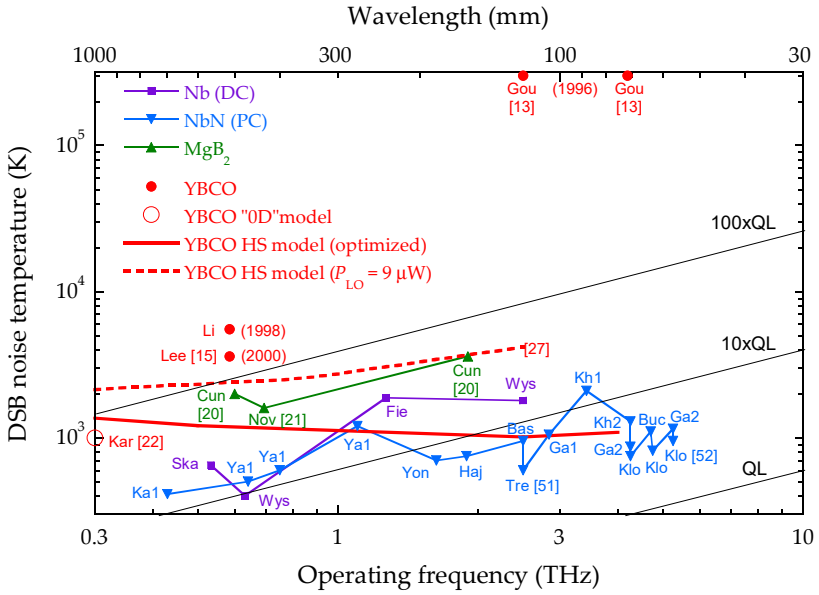

Figure 16. For HEB heterodyne receivers or mixers, double sideband noise temperature as a function of operating frequency. DC and PC are for diffusion cooled and phonon cooled devices, respectively. Hot spot (HS) model results are those of Table 2 (optimized) and Reference [27] (fixed LO power). QL: Quantum limit $h\nu/(2k_B)$. Redrawn and updated after [56] and [45].

As a corollary remark, we notice that the authors in Reference [24] applied a factor 0.3 to K_{RF} for an optimal fit between their noise simulations and measurements on NbN HEBs. After having applied this same correction in our model, we also checked a very good (and even better) fit with the noise temperature measurements reported in Reference [24]. In fact, our results benefited from computational software improvements: Fewer errors accumulated when solving the differential

equations, interpolation between points to obtain K_{DC}, and smoothing algorithms. The physical explanation for this overestimation of the resistance variation induced by the RF power remains, however, uncertain for the authors in Reference [24], and ourselves. These considerations nevertheless encouraged us to adapt the NbN HEB hot spot model to YBCO HEBs. Clearly the adjustment of the K_{RF} correction coefficient should require a comparative and systematic study with YBCO HEB mixer experimental tests, which is a potential point of progress in the present approach.

We finally comment on the availability of LO sources. Below 1 THz, the solid state based electronic sources (frequency multiplier chains) offer compactness, tunability and room temperature operation with, e.g., delivered $P_{LO} \approx 150$ μW at 750 GHz (see Reference [57] for instance). Up to 2.5 THz, another room temperature alternative relies on tunable backward wave oscillators (BWO). However, the operation of BWOs requires heavy weight magnets, making the BWOs bulky; they deliver, e.g., $P_{LO} \approx$ 25 μW at 2 THz (see Reference [58] for instance). At and above 2.5 THz, the LO power can be obtained from optoelectronic sources, such as compact mm-size THz quantum cascade lasers (QCL) operating at 70 K, with P_{LO} in the 50 μW to 1 mW range [59,60]. The temperature operation of 70 K, matching the HEB operation, makes it possible to integrate both components within similar cryogenic systems.

4.5. Standoff Detection Limits with YBCO HEB Mixers

We are discussing here the results on standoff detection requirements (Section 3.4) in the light of achievable noise performance (Sections 3.3 and 4.3). Figure 17a summarizes results presented in Section 3.4 by showing the dependence on the target distance of the standoff detection system in terms of required mixer noise temperature. Constraints of a high relative humidity level and transmission through a cotton tissue have been considered to match a realistic scenario, thus leading to reduce temperature resolution (i.e., increasing ΔT values) at higher frequencies. The higher d_T is expected, the lower T_{DSB} floor of the receiver system is required.

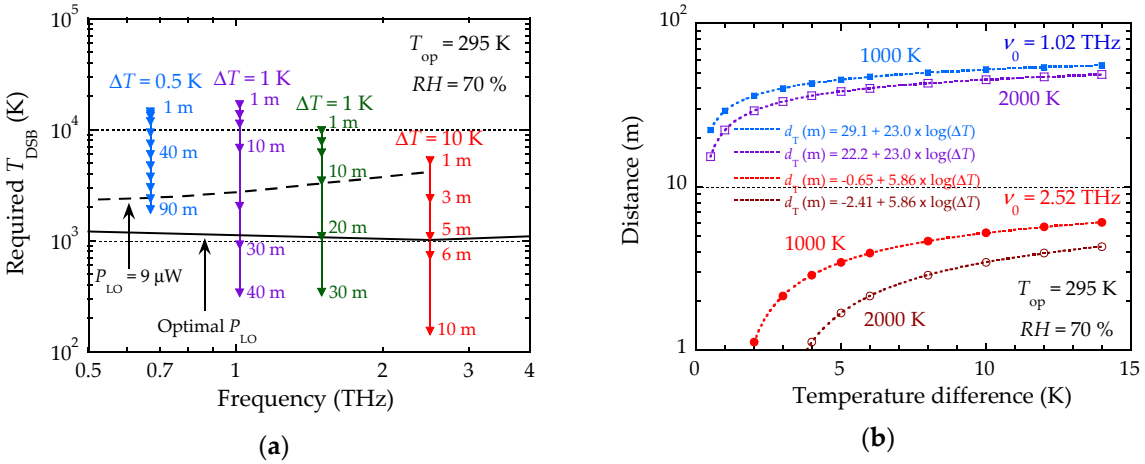

Figure 17. Standoff detection DSB requirements: (**a**) Required noise temperature as a function of ν_0 for various distances at specified ΔT and fixed humidity; simulated T_{DSB} values for device B are also shown at both optimal P_{LO} conditions - solid curve (Table 2) and at fixed P_{LO} = 9 μW - dashed curve [27]; (**b**) Required distance vs. temperature difference relationship to achieve T_{DSB} = 1000 K or 2000 K, at fixed RH. Symbols: Computed values, dotted curves: Best fits (according to functions indicated).

This latter point is emphasized in Figure 17b, which exhibits the d_T vs. ΔT relationship illustrating a constant T_{DSB} value. T_{DSB} values were chosen at 1000 K and at 2000 K, corresponding to an optimal operating point (in terms of local oscillator power in particular) for YBCO device B, as shown in Table 2. For instance, with a 2.5 THz receiver exhibiting T_{DSB} = 2000 K, we could expect $d_T \approx 3.5$ m at ΔT = 10 K.

However, if the HEB mixer operates at a non-optimal point, e.g., due to a low available LO power (e.g., P_{LO} = 9 μW), the mixer noise temperature increases (see values of $T_{DBS\text{-}MIN}$ in Table 5, extracted from Reference [27]). In this context of non-optimal operating point, Table 5 presents various potential scenarios for accommodating the HEB mixer performance at three frequencies. Calculations were also performed by relaxing the obstacle attenuation constraint. As an example, for a 2.5 THz receiver exhibiting T_{DSB} = 4150 K, we should expect $d_T \approx 1.6$ m at ΔT = 10 K and RH = 70%. If the obstacle transmission parameter is relaxed (t_{obs} = 1), the achievable target distance increases: For the same receiver, we could expect $d_T \approx 11.5$ m at ΔT = 10 K and RH = 70%.

Table 5. Standoff detection scenarios (with and without obstacle) designed to accommodate YBCO HEB mixer performance (device B) in terms of minimum T_{DSB} at P_{LO} = 9 μW [27].

Frequency (THz)	$T_{DSB\text{-}MIN}$ (K) [27]	Obstacle	ΔT (K)	RH (%)	D_T (m)	NEP (fW/Hz$^{1/2}$)	T_{DSB} (K)
0.67	2480 [1]	Yes	0.5	70	78	3.1	2495
0.67	2480 [1]	No	0.5	70	90.8	3.1	2485
1.02	2730	Yes	1.0	70	19.0	3.4	2760
1.02	2730	No	1.0	70	26.5	3.4	2775
2.52	4150	Yes	10	30	3.8	5.1	4160
2.52	4150	Yes	10	70	1.6	5.1	4150
2.52	4150	No	10	70	11.5	5.2	4245

[1] Simulated at 750 GHz.

As a final comment, we compare the chosen instantaneous bandwidth $\Delta\nu$ = 1 GHz to the expected HEB IF cutoff related to the phonon escape time (Figure 10, Section 3.3.3). This choice is close to the simulated bandwidth for device A. For device B, however, the expected bandwidth approaches ~200 MHz, which falls short of the standoff mixer bandwidth parameter. However, it should be emphasized that measurements of YBCO-based devices have exhibited several GHz bandwidth values (e.g., 7 GHz [15]). This discrepancy could be ascribed to a vortex flow mechanism, also invoked to interpret YBCO detectors response, which would superimpose to the regular HEB action, leading to an improved bandwidth value [12].

5. Conclusions and Future Plans

Our first contribution in this paper was to provide a physical description of the superconducting transition enabling to introduce the YBCO THz conductivity in the HEB equations solving loop. This description allowed us to have access to the full impedance of the nano-constriction as a function of temperature, highlighting in particular: (i) The shift and broadening of the superconducting transition as the THz frequency increases, (ii) a residual resistance in the low temperature limit. The knowledge of this impedance also allowed to introduce the THz power matching factor with the antenna, thus leading to a relevant discussion on the influence of the LO power level to optimize the HEB performance.

Our second contribution was to approach in a realistic way the LO power dissipation in the constriction, by making the assumption of a uniform current along this constriction, as delivered by the antenna. The resulting non-uniform LO power dissipation along the constriction, in the frame of a hot spot model, has a clear influence on the shape of the DC *I-V* plots that gave us the opportunity to check our simulations with published measurement results.

Our third contribution was to simulate the gain, noise temperature and IF bandwidth of an HEB THz mixer. The presentation of the results in the form of level maps in P_{DC} vs. P_{LO} coordinates made it possible to clearly illustrate the optimal operating conditions as a function of the THz frequency for a YBCO HEB. For instance, it was shown that $T_{DSB} \approx 1000$ K could ultimately be achieved at $P_{LO} \approx 13$ μW for a constriction of dimensions compatible with our technological process. The IF instantaneous bandwidth was shown to lie below 1 GHz for a 10 nm thick YBCO constriction, and to be

roughly inversely proportional to the thickness. Some comparisons with the few available published results could be made. It has been noted that some flux flow effect could be involved in the detection mechanism and increase the bandwidth, which is a point to be further considered. These models will also provide a useful guide to refine our ongoing HEB fabrication process.

Our fourth contribution consisted in evaluating the performances required to implement a YBCO HEB in a standoff detection system in passive mode. The knowledge of the optimized performances of the HEB made it possible to discuss the conditions of detection (at the diffraction limit) according to the parameters of the standoff system (distance to the target, absorption and atmospheric humidity, temperature resolution, obstacles). The impact of non-optimized conditions (with respect to P_{LO} level) was also discussed. Typically, detection at 3 m through cotton cloth could be readily achieved in moderate humidity conditions with 10 K target temperature resolution.

This set of modeling studies will support ongoing new imager design and evaluation. Future work will include the development of a 2.5 THz coherent detection system prototype, based on a YBCO HEB mixer as a heterodyne detector and a QCL source as a local oscillator, each device being implemented in its own cryostat or, even better, in its own miniaturized cryo-generator [61]. The main challenges concern: (i) The production of high quality *c*-axis oriented YBCO ultrathin films and antenna-coupled nano-constrictions made from these films, which are particularly sensitive to technological steps; (ii) the implementation of a THz LO source of sufficient power, while limiting its thermal dissipation; (iii) the development of a low noise/broadband cooled IF amplifier chain; (iv) the implementation of optical components in the cryostats; (v) the consideration of an adequate strategy for the imaging system with YBCO HEB mixers, e.g., scanning vs. staring array options.

Author Contributions: Conceptualization, R.L., A.D., V.J. and A.K.; methodology, R.L.; formal analysis, R.L. and V.J.; investigation, R.L., A.D., V.J. and A.K.; visualization, R.L., A.K. and A.D.; writing—original draft preparation, A.K.; writing—review and editing, A.K., A.D. and V.J.; supervision, A.K.; project administration, A.D. and A.K.; funding acquisition, A.D.

Funding: This research was part of the MASTHER project, funded by the French National Research Agency under grant # 2011-BS03-008-01.

Acknowledgments: The authors wish to thank Dr. Juliane Raasch (KIT, Karlsruhe, Germany) to have kindly provided measurement results on YBCO nano-constrictions.

Conflicts of Interest: The authors declare no conflict of interest.

References

1. Gershenzon, E.M.; Gol'tsman, G.N.; Gousev, Y.P.; Elant'ev, A.I.; Semenov, A.D. Electromagnetic radiation mixer based on electron heating in resistive state of superconductive Nb and YBCO films. *IEEE Trans. Magn.* **1991**, *27*, 1317–1320. [CrossRef]
2. Shukarov, A.; Lobanov, Y.; Gol'tsman, G. Superconducting hot-electron bolometer: From the discovery of hot-electron phenomena to practical applications. *Supercond. Sci. Technol.* **2016**, *29*, 023001. [CrossRef]
3. Karasik, B.S.; McGrath, W.R.; Wyss, R.A. Optimal Choice of Material for HEB Superconducting Mixers. *IEEE Trans. Appl. Supercond.* **1999**, *9*, 4213–4216. [CrossRef]
4. Karasik, B.S.; Sergeev, A.V.; Prober, D.E. Nanobolometers for THz Photon Detection. *IEEE Trans. Terahertz Sci. Technol.* **2011**, *1*, 97–111. [CrossRef]
5. Maezawa, H. Application of Superconducting Hot-Electron Bolometer Mixers for Terahertz-Band Astronomy. *IEICE Trans. Electron.* **2015**, *E98-C*, 196–206. [CrossRef]
6. Lindgren, M.; Currie, M.; Williams, C.; Hsiang, T.Y.; Fauchet, P.M.; Sobolewski, R. Intrinsic picosecond response time of Y-Ba-Cu-O superconducting photodetectors. *Appl. Phys. Lett.* **1999**, *74*, 853–855. [CrossRef]
7. Garcés-Chávez, V.; De Luca, A.; Gaugue, A.; Georges, P.; Kreisler, A.; Brun, A. Temporal response of high-temperature superconductor thin-film using femtosecond pulses. In Proceedings of the 4th European Conference on Applied Superconductivity, Sitges, Spain, 14–17 September 1999; Obradors, X., Ed.; Institute of Physics: Bristol, UK, 2000; pp. 93–96.

8. Thoma, P.; Raasch, J.; Scheuring, A.; Hofherr, M.; Il'in, K.; Wünsch, S.; Semenov, A.; Hübers, H.-W.; Judin, V.; Müller, A.-S.; et al. Highly responsive Y-Ba-Cu-O Thin Film THz Detectors With Picosecond Time Resolution. *IEEE. Trans. Appl. Supercond.* **2013**, *23*, 2400206. [CrossRef]
9. Li, C.T.; Deaver, B.S., Jr.; Lee, M.; Weikle, R.M., II; Rao, R.A.; Eom, C.B. Gain bandwidth and noise characteristics of millimeter-wave $YBa_2Cu_3O_7$ hot-electron bolometer mixers. *Appl. Phys. Lett.* **1998**, *73*, 1727–1929. [CrossRef]
10. Harnack, O.; Beuven, S.; Darula, M.; Kohlstedt, H.; Tarasov, M.; Stephanson, E.; Ivanov, Z. HTS mixers based on the Josephson effect and on the hot-electron bolometric effect. *IEEE Trans. Appl. Supercond.* **1999**, *9*, 3765–3768. [CrossRef]
11. Uchida, T.; Yazaki, H.; Yasuoka, Y.; Suzuki, K. Slot antenna coupled $YBa_2Cu_3O_{7-\delta}$ hot-electron bolometers for millimeter-wave radiation. *Phys. C* **2001**, *357–360*, 1596–1599. [CrossRef]
12. Il'in, K.S.; Siegel, M. Microwave mixing in microbridges made from YBCO thin films. *J. Appl. Phys.* **2002**, *92*, 361–369. [CrossRef]
13. Gousev, Y.P.; Semenov, A.D.; Nebosis, R.S.; Pechen, E.V.; Varlashkin, A.V.; Renk, K.F. Broad-band coupling of THz radiation to $YBa_2Cu_3O_{7-\delta}$ hot-electron bolometer mixer. *Supercond. Sci. Technol.* **1996**, *9*, 779–787. [CrossRef]
14. Cherednichenko, S.; Rönnung, F.; Gol'tsman, G.; Kollberg, E.; Winkler, D. $YBa_2Cu_3O_{7-\delta}$ hot-electron bolometer mixer at 0.6 THz. *Proc. Int. Symp. Space Terahertz Technol.* **2000**, 526–531.
15. Lee, M.; Li, R.C.-T. Wide bandwidth far-infrared mixing using a high-T_c superconducting bolometer. In Proceedings of the 8th International Conference on Terahertz Electronics, Darmstadt, Germany, 28–29 September 2000; pp. 99–101.
16. Kreisler, A.J.; Dégardin, A.F.; Aurino, M.; Péroz, C.; Villegier, J.-C.; Beaudin, G.; Delorme, Y.; Redon, M.; Sentz, A. New trend in terahertz detection: High-T_c superconducting hot electron bolometer technology may exhibit advantages vs. low-T_c devices. In Proceedings of the 2007 IEEE/MTT-S International Microwave Symposium, Honolulu, HI, USA, 3–8 June 2007; pp. 345–348. [CrossRef]
17. Harrabi, K.; Cheenne, N.; Chibane, F.; Boyer, F.; Delord, P.; Ladan, F.-R.; Maneval, J.-P. Thermal boundary resistance of $YBa_2Cu_3O_7$ on MgO films deduced from the transient $V(I)$ response. *Supercond. Sci. Technol.* **2000**, *13*, 1222–1226. [CrossRef]
18. Ladan, F.-R.; Harrabi, K.; Rosticher, M.; Mathieu, P.; Maneval, J.-P.; Villard, C. Current-temperature diagram of resistive states in long superconducting niobium filaments. *J. Low Temp. Phys.* **2008**, *153*, 103–122. [CrossRef]
19. Harnack, O.; Il'in, K.S.; Siegel, M.; Karasik, B.S.; McGrath, W.R.; de Lange, G. Dynamics of the response to microwave radiation in $YBa_2Cu_3O_{7-x}$ hot-electron bolometer mixers. *Appl. Phys. Lett.* **2001**, *79*, 1906–1908. [CrossRef]
20. Cunnane, D.; Kawamura, J.H.; Wolak, M.A.; Acharya, N.; Xi, X.X.; Karasik, B.S. Optimization of Parameters of MgB_2 Hot-Electron Bolometers. *IEEE Trans. Appl. Supercond.* **2017**, *27*, 2300405. [CrossRef]
21. Novoselov, E.; Cherednichenko, S. Broadband MgB_2 Hot-Electron Bolometer Mixers Operating up to 20 K. *IEEE Trans. Appl. Supercond.* **2017**, *27*, 2300504. [CrossRef]
22. Karasik, B.S.; McGrath, W.R.; Gaidis, M.C. Analysis of a high-T_c hot-electron superconducting mixer for terahertz applications. *J. Appl. Phys.* **1997**, *81*, 1581–1589. [CrossRef]
23. Adam, A.; Gaugue, A.; Ulysse, C.; Kreisler, A.; Boulanger, C. Three-temperature model for hot electron superconducting bolometers based on high-T_c superconductor for terahertz applications. *IEEE Trans. Appl. Supercond.* **2003**, *13*, 155–159. [CrossRef]
24. Khosropanah, P.; Merkel, H.; Yngvesson, S.; Adam, A.; Cherednichenko, S.; Kollberg, E. A distributed device model for phonon-cooled HEB mixers predicting IV characteristics, gain, noise and IF bandwidth. In Proceedings of the 11th International Symposium on Space Terahertz Technology, University of Michigan, Ann Arbor, MI, USA, 1–3 May 2000; pp. 474–488.
25. Ladret, R.G.; Dégardin, A.F.; Kreisler, A.J. Nanopatterning and hot spot modeling of YBCO ultrathin film constrictions for THz mixers. *IEEE Trans. Appl. Supercond.* **2013**, *23*, 2300305. [CrossRef]
26. Ladret, R.G.; Kreisler, A.J.; Dégardin, A.F. High-T_C micro and nano-constrictions modeling: Hot spot approach for DC characteristics and HEB THz mixer performance. *J. Phys. Conf. Ser.* **2014**, *507*, 042020. [CrossRef]

27. Ladret, R.G.; Kreisler, A.J.; Dégardin, A.F. YBCO-Constriction Hot Spot Modeling: DC and RF Descriptions for HEB THz Mixer Noise Temperature and Conversion Gain. *IEEE Trans. Appl. Supercond.* **2015**, *25*, 2300505. [CrossRef]
28. Ma, J.-G.; Wolff, I. Modeling the microwave properties of superconductors. *IEEE Trans. Microw. Theory Technol.* **1995**, *43*, 1053–1059. [CrossRef]
29. Ma, J.-G.; Wolff, I. Electromagnetics in high-T_c superconductors. *IEEE Trans. Microw. Theory Technol.* **1996**, *44*, 537–542. [CrossRef]
30. Péroz, C.; Villégier, J.-C.; Dégardin, A.F.; Guillet, B.; Kreisler, A.J. High critical current densities observed in $PrBa_2Cu_3O_{7-\delta}/YBa_2Cu_3O_{7-\delta}/PrBa_2Cu_3O_{7-\delta}$ ultrathin film constrictions. *Appl. Phys. Lett.* **2006**, *89*, 142502. [CrossRef]
31. Gao, J.-R.; Yagoubov, P.A.; Klapwijk, T.M.; de Korte, P.A.J.; Ganzevles, W.F.; Floet, D.W. Development of THz Nb diffusion-cooled hot electron bolometer mixers. *Proc. SPIE Conf.* **2003**, *4855*, 371–382. [CrossRef]
32. Kollberg, E.L.; Yngvesson, K.S.; Ren, Y.; Zhang, W.; Gao, J.-R. Impedance of hot-electron bolometer mixers at terahertz frequencies. *IEEE Trans. Terahertz Sci. Technol.* **2011**, *1*, 383–389. [CrossRef]
33. Miao, W.; Zhang, W.; Zhong, J.Q.; Shi, S.C.; Delorme, Y.; Lefevre, R.; Feret, A.; Vacelet, T. Non-uniform absorption of terahertz radiation on superconducting hot electron bolometer microbridges. *Appl. Phys. Lett.* **2014**, *104*, 052605. [CrossRef]
34. Abbott, F.; Dégardin, A.F.; Kreisler, A.J. YBCO thin film sputtering: An efficient way to promote microwave properties. *IEEE Trans. Appl. Supercond.* **2005**, *15*, 2907–2910. [CrossRef]
35. Grossman, E.-N. Lithographic antennas for submillimeter and infrared frequencies. In Proceedings of the IEEE International Symposium on Electromagnetic Compatibility, Atlanta, GA, USA, 14–18 August 1995; Volume 14–18, pp. 102–107.
36. Türer, I.; Dégardin, A.F.; Kreisler, A.J. UWB Antennas for CW Terahertz Imaging: Geometry Choice Criteria. In *Ultra-Wideband, Short-Pulse Electromagnetics 10*; Sabath, F., Mokole, E.L., Eds.; Springer: New York, NY, USA, 2014; pp. 463–472. ISBN 978-1-4614-9499-7.
37. Karasik, B.S.; Elantiev, A.I. Noise temperature limit of a superconducting hot-electron bolometer mixer. *Appl. Phys. Lett.* **1996**, *68*, 853–855. [CrossRef]
38. Semenov, A.D.; Hubers, H.-W. Bandwidth of a hot-electron bolometer mixer according to the hot spot model. *IEEE Trans. Appl. Supercond.* **2001**, *11*, 196–199. [CrossRef]
39. Rieke, G.H. Visible and infrared coherent receivers. In *Detection of Light: From the Ultraviolet to the Submillimeter*, 2nd ed.; Cambridge University Press: New York, NY, USA, 2003; pp. 275–301, ISBN-13: 978-0-511-06518-7.
40. Wallace, B. Analysis of RF imaging applications at frequencies over 100 GHz. *Appl. Opt.* **2010**, *49*, E38–E47. [CrossRef] [PubMed]
41. Slocum, D.M.; Goyette, T.M.; Slingerland, E.J.; Giles, R.H.; Nixon, W.E. Terahertz atmospheric attenuation and continuum effects. *Proc. SPIE Conf.* **2013**, *8716*, 871607. [CrossRef]
42. Beno, M.A.; Soderholm, L.; Capone, D.W., II; Hinks, D.G.; Jorgensen, J.D.; Grace, J.D.; Schuller, I.K.; Segre, C.U.; Zhang, K. Structure of the single-phase high-temperature superconductor $YBa_2Cu_3O_{7-\delta}$. *Appl. Phys. Lett.* **1987**, *51*, 57–59. [CrossRef]
43. Streiffer, S.K.; Zielinski, E.M.; Lairson, B.M.; Bravman, J.C. Thickness dependence of the twin density in $YBa_2Cu_3O_{7-\delta}$ thin films sputtered onto MgO substrates. *Appl. Phys. Lett.* **1991**, *58*, 2171–2173. [CrossRef]
44. Kreisler, A.; Dégardin, A.; Guillet, B.; Villégier, J-C.; Chaubet, M. High-Tc Superconducting Hot Electron Bolometers for Terahertz Mixer Applications. In Proceedings of the 9th World Multi-Conference on Systemics, Cybernetics and Informatics, Orlando, FL, USA, 10–13 July 2005; pp. 165–217.
45. Ladret, R.G.; Kreisler, A.J.; Dégardin, A.F. Terahertz superconducting hot electron bolometers: Technological issues and predicted mixer performance for Y-Ba-Cu-O devices. *Proc. SPIE Conf.* **2014**, *9252*, 92520R. [CrossRef]
46. Goyette, T.M.; Dickinson, J.C.; Linden, K.J.; Neal, W.R.; Joseph, C.S.; Gorveatt, W.J.; Waldman, J.; Giles, R.; Nixon, W.E. 1.56 Terahertz 2-frames per second standoff imaging. *Proc. SPIE Conf.* **2008**, *6893*, 68930J. [CrossRef]
47. Puc, U.; Abina, A.; Rutar, M.; Zidansek, A.; Jeglic, A.; Valusis, G. Terahertz spectroscopic identification of explosive and drug simulants concealed by various hiding techniques. *Appl. Opt.* **2015**, *54*, 4495–4502. [CrossRef] [PubMed]

48. Raash, J. Electrical-Field Sensitive $YBa_2Cu_3O_{7-x}$ Detectors for Real-Time Monitoring of Picosecond THz Pulses. Doktor-Ingenieur Thesis, Karlsruhe Institut für Technologie (KIT), Karlsruhe, Germany, August 2017. Available online: https://publikationen.bibliothek.kit.edu/1000073798 (accessed on 24 January 2019).
49. Ladret, R. Nano-Mélangeurs Bolométriques Supraconducteurs à Electrons Chauds en Y-Ba-Cu-O Pour Récepteur Térahertz en Mode Passif. PhD Thesis, Université Pierre et Marie Curie, Paris, France, July 2016. Available online: https://tel.archives-ouvertes.fr/tel-01832519/document (accessed on 15 Ianuary 2019). (In French)
50. Schmid, A.; Raasch, J.; Kuzmin, A.; Steinmann, J.L.; Wuensch, S.; Arndt, M.; Siegel, M.; Müller, A.-S.; Cinque, G.; Frogley, M.D. An Integrated Planar Array of Ultrafast THz Y–Ba–Cu–O Detectors for Spectroscopic Measurements. *IEEE Trans. Appl. Supercond.* **2017**, *27*, 2200105. [CrossRef]
51. Tretyakov, I.; Ryabchun, S.; Finkel, M.; Maslennikova, A.; Kaurova, N.; Lobastova, A.; Voronov, B.; Gol'tsman, G. Low noise and wide bandwidth of NbN hot-electron bolometer mixers. *Appl. Phys. Lett.* **2011**, *98*, 033507. [CrossRef]
52. Kloosterman, J.L.; Hayton, D.J.; Ren, Y.; Kao, T.-Y.; Hovenier, N.; Gao, J.-R.; Klapwijk, T.M.; Hu, Q.; Walker, C.K.; Reno, J.L. Hot electron bolometer heterodyne receiver with a 4.7-THz quantum cascade laser as a local oscillator. *Appl. Phys. Lett.* **2013**, *102*, 011123. [CrossRef]
53. Wolak, M.A.; Acharya, N.; Tan, T.; Cunnane, D.; Karasik, B.S.; Xi, X. Fabrication and Characterization of Ultrathin MgB_2 Films for Hot-Electron Bolometer Applications. *IEEE Trans. Appl. Supercond.* **2015**, *25*, 7500905. [CrossRef]
54. Arpaia, R.; Ejrnaes, M.; Parlato, L.; Tafuri, F.; Cristiano, R.; Golubev, D.; Sobolewski, R.; Bauch, T.; Lombardi, F.; Pepe, G.P. High-temperature superconducting nanowires for photon detection. *Phys. C* **2015**, *509*, 16–21. [CrossRef]
55. Lyatti, M.; Savenko, A.; Poppe, U. Ultra-thin $YBa_2Cu_3O_{7-x}$ films with high critical current density. *Supercond. Sci. Technol.* **2016**, *29*, 065017. [CrossRef]
56. Kreisler, A.; Gaugue, A. Recent progress in HTSC bolometric detectors: From the mid-infrared to the far-infrared (THz) range. *Supercond. Sci. Technol.* **2000**, *13*, 1235–1245. [CrossRef]
57. Vadiodes. Available online: http://www.vadiodes.com/en/frequency-multipliers (accessed on 14 January 2019).
58. Microtech Inst. Available online: http://mtinstruments.com/THz_Generators.html (accessed on 14 January 2019).
59. Ravarro, M.; Jagtap, V.; Santarelli, G.; Sirtori, C.; Li, L.; Khanna, S.P.; Linfield, E.; Barbieri, S. Continuous-wave coherent imaging with terahertz quantum cascade lasers using electro-optic harmonic sampling. *Appl. Phys. Lett.* **2013**, *102*, 091107. [CrossRef]
60. Wang, T.; Liu, J.; Liu, F.; Wang, L.; Zhang, J.; Wang, Z. High-Power Single-Mode Tapered Terahertz Quantum Cascade Lasers. *IEEE Photonics Technol. Lett.* **2015**, *27*, 1492–1494. [CrossRef]
61. Masther Research Project Funded by the French National Research Agency under Grant # 2011-BS03-008-01. Information. Available online: http://www.agence-nationale-recherche.fr/suivi-bilan/editions-2013-et-anterieures/recherches-exploratoires-et-emergentes/blanc-generalite-et-contacts/blanc-presentation-synthetique-du-projet/?tx_lwmsuivibilan_pi2%5BCODE%5D=ANR-11-BS03-0008 (accessed on 14 January 2019). (In French)